Research Square

Preprints are preliminary reports that have not undergone peer review.
They should not be considered conclusive, used to inform clinical practice,
or referenced by the media as validated information.

Hidden-driver inference reveals synergistic brain-penetrant therapies for medulloblastoma

Jiyang Yu

Jiyang.Yu@stjude.org

St. Jude Children's Research Hospital https://orcid.org/0000-0003-1244-4429

jingjing liu

St. Jude Children's Research Hospital, USA https://orcid.org/0000-0002-8184-8382

Xu Yang

St. Jude Children's Research Hospital https://orcid.org/0000-0002-0398-1436

Mingrui Zhu

St. Jude Children's Research Hospital

Xinran Dong

Key Laboratory of Birth Defects, Children's Hospital, Fudan University and Institutes of Biomedical Sciences, Fudan University, Shanghai 201102 https://orcid.org/0000-0001-9868-8795

Honglei Zhou

St. Jude Children's Research Hospital

Brandon Bianski

St. Jude Children's Research Hospital

Barbara Jonchere

St. Jude Children's Research Hospital

Wenwei Lin

St. Jude Children's Research Hospital https://orcid.org/0000-0001-8754-6150

Xiang Fu

St. Jude Children's Research Hospital

Lei Yang

St. Jude Children's Research Hospital https://orcid.org/0000-0002-3060-0790

Burgess Freeman

St. Jude Children's Research Hospital https://orcid.org/0000-0003-2174-5119

Abigail Wang

St. Jude Children's Research Hospital

Ruilin Jiang

St. Jude Children's Research Hospital

Taosheng Chen

St. Jude Children's Research Hospital https://orcid.org/0000-0001-6420-3809

Giles Robinson
St. Jude Children's Research Hospital https://orcid.org/0000-0001-7441-9486
Martine Roussel
St. Jude Children's Research Hospital https://orcid.org/0000-0002-1740-8139
Thomas Merchant
St. Jude Children's Research Hospital https://orcid.org/0000-0002-0412-6255
Amar Gajjar
St. Jude Children's Research Hospital https://orcid.org/0000-0001-5019-0699

Article

Keywords:

Posted Date: March 6th, 2026

DOI: https://doi.org/10.21203/rs.3.rs-8278592/v1

License: This work is licensed under a Creative Commons Attribution 4.0 International License.
Read Full License

Additional Declarations: There is **NO** Competing Interest.

Hidden-driver inference reveals synergistic brain-penetrant therapies for medulloblastoma

Jingjing Liu[1,10], Xu Yang[1,10], Mingrui Zhu[1,10], Xinran Dong[2], Honglei Zhou[1], Brandon Bianski[3], Barbara M. Jonchere[4], Wenwei Lin[5], Xiang Fu[6], Lei Yang[6], Burgess B. Freeman III[7], Abigail S. Wang[1], Ruilin Jiang[1], Taosheng Chen[5], Giles W. Robinson[8], Martine F. Roussel[4], Thomas E. Merchant[3], Amar Gajjar[8,9], Jiyang Yu[1,*]

[1]Department of Computational Biology, St. Jude Children's Research Hospital, Memphis, TN 38105, USA

[2]Center for Molecular Medicine, Children's Hospital of Fudan University, Shanghai 201102, P.R. China

[3]Department of Radiation Oncology, St Jude Children's Research Hospital, Memphis, TN 38105, USA

[4]Department of Tumor Cell Biology, St Jude Children's Research Hospital, Memphis, TN 38105, USA

[5]Department of Chemical Biology and Therapeutics, St Jude Children's Research Hospital, Memphis, TN 38105, USA

[6]Analytical Technologies Center, Department of Chemical Biology and Therapeutics, St Jude Children's Research Hospital, Memphis, TN 38105, USA

[7]Preclinical Pharmacokinetics Shared Resource, St Jude Children's Research Hospital, Memphis, TN 38105, USA

[8]Department of Oncology, St. Jude Children's Research Hospital, Memphis, TN, 38105, USA

[9]Department of Pediatric Medicine, Department of Oncology, St Jude Children's Research Hospital, Memphis, TN 38105, USA

[10]: These authors contributed equally

[*]Correspondence: jiyang.yu@stjude.org

ABSTRACT

Effective therapies for high-risk medulloblastoma (MB), particularly MYC-driven Group 3 (G3) MB, remain elusive due to limited druggable mutations, poor blood–brain barrier (BBB) penetration, and rapid resistance. We developed **SINBA (Synergy Inference by Data-driven Network-Based Bayesian Analysis)**, a systems biology framework that predicts synergistic, BBB-permeable drug combinations by identifying *hidden drivers* that sustain oncogenic programs without detectable genetic or transcriptional alterations. Integrating MB-specific gene networks, transcriptomic data, and drug–gene interactions, SINBA prioritized 32 candidate combinations, of which 19 were experimentally validated as synergistic. The **MEK inhibitor mirdametinib** and **p38 inhibitor regorafenib** emerged as the top brain-penetrant pair, suppressing G3 MB progression and extending survival in human xenograft and immunocompetent mouse models, with efficacy enhanced by low-dose radiation. Single-cell analysis revealed selective targeting of the **developmental origins of G3 MB**, accompanied by immune microenvironment reprogramming. These findings establish *hidden-driver inference* as a generalizable framework for rational drug combination discovery.

INTRODUCTION

Brain tumors are the most common pediatric solid tumor, producing more deaths in children under the age of 20 than any other pediatric cancer[1]. Among them, the most prevalent is medulloblastoma (MB), an embryonal tumor of the cerebellum that consists of four distinct molecular subtypes: WNT, SHH, Group 3 (G3), and Group 4 (G4)[2, 3]. Despite the unique molecular and clinical characteristics of these subtypes, standard treatment for medulloblastoma follows a single protocol: maximal surgical resection followed by craniospinal irradiation and adjuvant chemotherapy. While these interventions have improved the 5-year survival rate to over 80% for average-risk patients,[4, 5] one in three high-risk MB patients will relapse within five years, and the survival rate for relapsed patients remains dismal[6, 7].

Common approaches to therapeutic discovery have yielded few clinically effective treatments for high-risk MB, due to both the nature of the disease and the limitations of current methods[8]. Most notably, few high-risk MB cases possess well-characterized druggable alterations—in fact, approximately 20% lack any identifiable genetic mutations—making the development of genomics-driven targeted therapies difficult[9]. High-throughput screening (HTS), though useful in research contexts, produces single agent therapies that may have poor blood-brain barrier (BBB) permeability, that are susceptible to rapid tumor resistance, and whose efficacy often depends on the relevance of the disease model used and the extent to which it recapitulates patient tumor biology.

The recent therapeutic success of combination therapies in certain cancers has generated widespread interest in drug combination screening[10, 11, 12, 13, 14, 15, 16, 17, 18]; however, standard experimental methods for combination screening are costly and limited in scale. Computational approaches[19, 20, 21, 22, 23, 24] (such as RECODR[22] or a graph-embedding machine learning approach

of single-cell transcriptomics data, DrugCell[24] or the community-developed approaches generated by the DREAM Consortium) have been developed to circumvent these limitations, but their utility in G3 MB is limited by, for example, the nature of their training datasets or their pan-cancer design.

Although few clinically actionable genes have been identified for MB[25], previous studies have identified cancer driver genes that, rather than possess genetic mutations, are functionally dysregulated through epigenetic modifications or post-translational alterations[26, 27, 28, 29, 30]. Such "hidden" drivers could be effective therapeutic targets; however, their lack of genetic mutation makes them more challenging to identify. We therefore developed SINBA, an end-to-end workflow that uses network-based Bayesian analysis to identify putative bottleneck drivers and then, based on those drivers, suggests potential therapeutic drug combinations. This approach addresses two of the major challenges of therapeutic discovery in MB: identifying druggable targets and reducing the candidate drug pool for combination screening.

In this study, we applied SINBA to G3 medulloblastoma, leveraging the transcriptomic data of three medulloblastoma patient cohorts. After validating the synergistic effects of SINBA-predicted drug combinations through *in vitro* HTS, we tested the efficacy of the top-ranked combination (regorafenib and a MEK inhibitor) in preclinical studies using both human xenografts and immunocompetent syngeneic murine G3 MB models. Combining regorafenib-MEK inhibitor treatment with low-dose irradiation improved cancer cell killing, supporting the potential benefit of incorporating these agents into standard MB therapy. Single-cell RNA sequencing (scRNA-seq) analysis revealed elevated driver activity and enhanced drug sensitivity scores in tumor cells that transcriptomically resemble early Unipolar Brush Cell (UBC) progenitors (henceforth "early UBC progenitor-like cells"), suggesting susceptibility to this combination therapy. Critically, this combination profoundly remodeled the tumor microenvironment (TME) in an immunocompetent

syngeneic mouse model, demonstrating both direct and immunomodulatory tumor suppression effects.

RESULTS

Nominating synergistic brain-penetrant drug combinations for G3 MB using SINBA, a hidden-driver-based computational framework

SINBA is a network-based algorithm that unbiasedly predicts synergistic drug combinations based on subtype-specific drivers. Broadly, the SINBA workflow proceeds as follows: users leverage a disease-specific gene-gene interaction network to identify drivers upregulated in a selected cancer subtype; these drivers are then filtered for druggability and provided as input to the SINBA software. SINBA then uses the interaction network and a drug-target database to design HTS experiments, the results of which are fed back into the software as additional input. Using these data, SINBA matches the input drivers with other hub genes to produce gene pairs with synergistic activity; these driver pairs are translated into drug pairs for subsequent combination screening. Finally, the results of combination screening are analyzed for synergy using a third-party algorithm, SynergyFinder[31, 32]; the drug pairs are then ranked according to their synergy. It should be noted that driver selection and driver-drug pairing are interdependent, concurrent processes. For example, the input drivers are used to select drugs for HTS, but then the results of HTS are used to further refine the list of drivers.

Using the G3 subtype of MB as a proof-of-concept, we describe the SINBA workflow in greater detail below (**Fig. 1a**):

Preparatory Steps

To equip SINBA to select synergistic drug pairs with good blood-brain barrier permeability, we generated a Brain Penetrant drug-target database (BPdb) consisting of 1,084 potential brain-penetrant agents (targeting 2,476 genes) (**Fig. 1b**). The BPdb expands substantially on the B3DB[33], a database of rigorously validated brain-penetrating compounds, by including additional, potentially-penetrating agents identified in the literature and clinical trials. Agents were presumed to be penetrants if they had been evaluated in neurotherapeutic trials or antibody-based modalities. 41% of the drugs in the BPdb were selected in this manner; overall, 59% of the drugs are FDA-approved. Five drug-gene interaction databases were used to annotate the targets in the BPdb: DrugBank[34], ChEMBL[35], cMAP[36], Repurposing Hub[37], and DGIdb[38, 39, 40] (**Fig. 1c; Supplementary Table 1**). Along with the BPdb, these drug-target databases were integrated into SINBA, supplying it with a comprehensive set of drugs and pharmacologically targetable genes to maximize generalizability outside of central nervous system tumors.

After compiling the BPdb, we pre-trained a disease-specific, gene-gene interaction network for medulloblastoma by applying SJARACNe[41], a mutual-information-based algorithm, to a dataset of 407 human MB patient transcriptome profiles (DKFZ_SJ)[25, 42, 43]. The resulting medulloblastoma interactome (MBi) captures the transcript-level interactions between transcription factor (TF) and signaling (SIG) genes[44]—the network hubs—and their predicted regulons. Altogether, the interactome comprised 1,567,381 interactions between 38,621 transcripts (corresponding to 15,317 genes); 12,495 of these transcripts belonged to TF and SIG hub genes (7,155 total).

Finally, we used the pretrained MBi and our NetBID2[45] algorithm to identify G3 MB-specific drivers, henceforth referred to as “seed” drivers. To do so, we superimposed the MBi onto the transcriptomic profiles of patients in the pretraining cohort plus two additional validation cohorts, GSE85217[46] and ICGC[9] (**Supplementary Table 2**), generating activity profiles for candidate TF and SIG drivers from the gene expression data. The activity inferred for each candidate driver

consisted of the expression of downstream targets weighted by the interaction strength. We then used NetBID2 to analyze the activity of the pretraining cohort, revealing 75 drivers that exhibited significantly higher activity in G3 MB compared to the other MB subgroups and normal cerebellum. Drivers for which there were no targeting drugs in the BPdb were discarded, leaving 45 druggable "seed drivers."

Comparison of the activity and expression profiles of these seed drivers in the two validation cohorts supports SINBA's activity-based approach to driver selection. Seed drivers were found to have consistent differential activity but not expression patterns across cohorts (**Supplementary Fig. 1a**), suggesting that activity data may be a more reliable measure of gene function. Data from the GSE85217 cohort, for which clinical outcomes were available, suggested that driver activity may also have greater clinical relevance. Analysis of the 42 drivers with matched activity and expression profiles in this cohort found patient survival to correlate significantly more with driver activity than with driver gene expression. For 67% of the drivers, there was a significant correlation between activity level and patient survival ($P < 0.05$); only 26% of the drivers showed a similar correlation for gene expression (**Supplementary Fig. 1b**; **Supplementary Table 3**). For example, the activity but not expression of BRAF and CDK7 significantly correlated with overall patient survival (**Supplementary Fig. 1c**). Compared to their RNA expression levels, these drivers' inferred activities had a cleaner pattern of elevation in G3 MB compared to the other medulloblastoma subtypes. Likewise, in an independent proteomics cohort of MB patient samples[47], there was an elevation in the phosphorylated protein activity of these genes despite their total protein levels remaining unchanged (**Supplementary Fig. 1d and 1e**).

Similarly, expression of MYC—whose activation is the hallmark of G3 MB—was insufficient to stratify risk groups in the GSE85217 cohort; on the other hand, there was a clear delineation in MYC *activity* between high- and low-risk MB (**Supplementary Fig. 1f**). Consistent with the

findings for BRAF and CDK7, MYC activity—but not total protein expression—was positively correlated with phospho-MYC levels in G3 MB tumors[47] (**Supplementary Fig. 1g**). These results demonstrate how activity-based approaches can be used to identify clinically relevant drivers that may evade discovery by conventional RNA and total protein expression analyses. To explore the drug databases, gene expression and patient survival data, and driver activities imputed in this study, we developed an interactive web application at https://yulab-stjude.shinyapps.io/SINBA_MB.

Nominating Synergistic Drug Pairs with SINBA Algorithm

Using the 45 seed drivers identified for G3 MB as input, SINBA predicted synergistic drug pairs for G3 MB in the following steps:

First, the software selected 69 drugs from the BPdb to undergo HTS, ensuring that each of the 45 seed drivers was a target gene for at least one drug. SINBA then used the results of screening these drugs in a G3 cell line (HDMB03) to select the top 20 most effective drugs with unique seed driver targets.

To identify synergistic partner genes for the 20 seed drivers, SINBA generated a list of candidate genes. It did this by filtering the hub genes from the MBi for druggability using the BPdb, yielding approximately 800 candidate "partner drivers". The candidate set was further refined by eliminating drivers that failed to demonstrate adequate synergy with any of the seeds. Candidate drivers were considered synergistic if their combined subnetwork with a seed driver yielded higher differential activity than either subnetwork alone. Driver synergy was measured using a custom statistical method that assigns a quantitative “synergy score” to driver pairs (see **Methods**). To select the final partners, SINBA used a greedy algorithm to determine which matrix of 20 seed drivers x 16 partner drivers would generate the highest collective synergistic score (**Fig. 1c**).

Next, SINBA selected a different drug for each of the 16 partner drivers, with preference given to drugs from the original library. If no suitable drug could be found in the original library, alternative drugs were selected from the BPdb; these drugs (21 in total) were then screened in the G3 cell line and the results used to select final partners for the remaining drivers. (For a summary of the HTS results of our combined libraries (90 drugs total), see **Supplementary Fig. 2a and 2b; Supplementary Table 4**). These 16 final partner drugs were then arranged in a matrix with the 20 seed drugs, producing 320 unique drug pairs for subsequent combination screening (**Fig. 1c**).

Drug Combination Screening and Synergy Analysis

Before proceeding to comprehensive drug combination screening, we assessed the potential synergy of our 320 drug pairs through a preliminary two-dose screening. Drugs were tested at EC_{20} (low dose) and EC_{50} (high dose) concentrations; drugs lacking EC_{20} or EC_{50} values were assigned the default values of 1 μM and 6 μM, respectively. This dual-dose strategy produced 1,280 unique drug-dose combinations for testing in the HDMB03 model. The efficacy of each drug-dose combination was quantified using a $\Delta\text{inhibition}_{mean}$ metric: the cell growth inhibition of a two-agent combination minus the mean of the inhibitions produced by using each agent alone at the same dose. Remarkably, 95% of the combinations tested produced efficacies greater than the mean of their parts (**Supplementary Fig. 2c**; **Supplementary Table 5**; see **Methods**).

For each drug-dose combination, we also calculated the $\Delta\text{inhibition}_{max}$, the difference in inhibition between the combination and whichever of its constituents produced greater inhibition alone. We then used this metric to select 32 candidate pairs that met one of the following four conditions: At the low-low dose, (1) combined inhibition >90% and $\Delta\text{inhibition}_{max}$ >10%, (2) combined inhibition >50% and $\Delta\text{inhibition}_{max}$ >15%, or (3) combined inhibition >80% and each single agent's

inhibition >70%; or, at any other dose-combination, (4) combined inhibition >50% and $\Delta\text{inhibition}_{max}$ >20%. These 32 drug pairs were advanced to the comprehensive screening step.

Drug pairs were comprehensively screened in HDMB03 cells using a 10 × 10 dose-response matrix, yielding 100 drug-dose combinations per pair. Screening was performed in triplicates. For each replicate matrix, we evaluated the synergy of each drug-dose combination using the Zero Interaction Potency (ZIP) model, a hybrid of the Loewe additivity and Bliss independence models[31, 32]; these values were then averaged to produce an overall ZIP score for the matrix. Each unique drug pair was assigned a ZIP score equalling the average of its three replicate matrices. Notably, 19 of the 32 drug pairs (59.4%) were found to be synergistic (ZIP score >0, **Fig. 1d**; **Supplementary Table 6**), confirming SINBA's effectiveness in identifying synergistic therapeutics.

Trametinib, a MEK inhibitor, and regorafenib, a multi-kinase inhibitor, emerged as the most synergistic drug pair. These drugs demonstrated profound synergy not only overall, but also in the low dose regions of their synergy score landscapes (**Supplementary Fig. 2d**).

Fine-tuning the drug pair for optimal BBB-penetrability

To confirm the blood-brain-barrier permeability of these drugs, we conducted preclinical pharmacokinetic studies for regorafenib in female CD-1 nude mice (see **Methods**). Following a single oral dose of regorafenib (10 mg/kg), we observed consistent plasma and brain concentrations, with inter- and intra-mouse coefficients of variation ranging from 7.7% to 28.6% (**Supplementary Fig. 3a**). Brain exposure was assessed by determining the unbound brain-to-plasma partition ratio ($K_{p,uu}$), a critical parameter in evaluating CNS drug penetration and distribution. Regorafenib demonstrated reasonable brain distribution ($K_{p,uu}$=0.143), which was consistent with prior murine studies, though slightly lower than previously reported 24-hour estimates[48]. Notably, regorafenib has also been shown to have a robust CNS exposure profile[49,

[50]. Similar methods[51] found trametinib to have a less favorable brain distribution ($K_{p,uu}$=0.069, **Supplementary Fig. 3b**). We therefore decided to include mirdametinib, another MEK inhibitor whose BBB-permeability has been established in the literature[52, 53], in our testing. Consistent with existing studies, we found mirdametinib to have a superior $K_{p,uu}$ of 0.243 (**Supplementary Fig. 3c**). Having confirmed regorafinib's BBB permeability and selected an additional MEK candidate, we advanced the regorafenib-MEK inhibitor combination to preclinical validation.

Regorafenib-MEK Inhibitor synergistic combination selectively kills G3 MB cells *in vitro*

Existing chemoproteomic profiling data has shown overlap between MEK inhibitors' targets and regorafenib's targets on the MAPK signaling pathway[54] (**Supplementary Fig. 3d**). This pathway (KEGG MAPK signaling[55]) is significantly upregulated in G3 tumors compared to normal cerebellum (**Supplementary Fig. 3e**), suggesting selective vulnerability in the G3 subtype. To better understand the mechanism underlying the synergy of MEK inhibitors and regorafenib, we expanded our testing to include an additional four G3 MB cell line models (D341, D425, D283, and MB002) as well as an SHH-MB cell line (DAOY with and without GFP).

First, we mapped the RNA-seq profiles of these cell lines[56] onto our MBi to generate paired activity profiles for MAPK11 (a subunit of p38 MAP kinase) and BRAF, the target drivers for regorafenib and trametinib/mirdametinib, respectively (**Fig. 2a**). We then calculated a signature for the trametinib/regorafenib combination using iLINCS[57] data on the drugs' gene expression signatures in a CNS-disease context. To do so, we used the activity profiles previously generated for each cell line to rank the drivers in each line by activity score. Using these rankings as a reference, we then calculated cell line-specific enrichment scores for the genes in which treatment with regorafenib or trametinib induced up- or down-regulation. These enrichment scores were used to calculate an integrated score for each cell line indicating its sensitivity to a trametinib-regorafenib combination (**Fig. 2a and Supplementary Fig. 4a**, see **Methods**).

These sensitivity predictions were largely born out in *in vitro* testing, where we used AlamarBlue cell viability assays to evaluate the regorafenib-trametinib and regorafenib-mirdametinib combinations in the MB cell lines. For each cell line, 80 drug-dose combinations were tested per drug pair (eight concentrations of MEK inhibitor and ten concentrations of regorafenib); the results were then used to calculate an overall ZIP score for each drug pair as previously.

Overall, the greatest collective synergy was observed in the D341 cell line, which ranked No. 1 for regorafenib/mirametinib and No. 2 for regorafenib/trametinib (**Fig. 2b and 2c**). Reasonable synergistic effects were also observed for both combinations in MB002 (**Fig. 2b and 2d**). As expected, no synergy was observed for these combinations in the SHH-MB line DAOY (**Supplementary Fig. 4b**). Despite being a G3 MB model, D425 was minimally responsive to both drug pairs, consistent with the low synergy score we had predicted for that cell line (**Supplementary Fig. 4c**). Some difference was observed in the performance of the drug pairs within a single cell line. For instance, the trametinib combination produced the highest synergy in D283, consistent with our predictions, whereas the mirdametinib combination produced no synergy in that line (**Fig. 2b and Supplementary Fig. 4d**).

To confirm the mechanism of action of regorafenib and the MEK inhibitors in the context of combination therapy, we compared the effects of combination therapy vs. monotherapy on signaling in three responsive G3 MB cell lines (D341, HDMB03, and MB002). For Western blot analysis, we selected three well-established targets of MEK inhibition (MEK, ERK, and BRAF), while for regorafenib—a multi-kinase inhibitor—we chose MAPK11/p38, regorafenib's main target in G3 MB according to our previous analysis with SINBA. Western blot analysis showed that the regorafenib-MEK inhibitor combinations reduced the phosphorylation levels of all four targets (MEK, ERK, BRAF, and p38), while total protein levels remained unchanged. In some cases,

combination therapy even produced a greater reduction in a target's phosphorylation compared to monotherapy. These findings confirmed effective on-target suppression of BRAF-MEK signaling by trametinib/mirdametinib and p38 signaling by regorafenib in G3 MB tumor cells in the contexts of both mono- and combination therapy (**Fig. 2e**).

Together, these *in vitro* studies confirmed the synergistic killing effect of regorafenib-MEK inhibitor combinations on G3 MB but not SHH-MB cells.

Regorafenib-MEK inhibitor combinations are effective for G3 MB *in vivo*

Having identified D341 as the cell line most likely to be sensitive to the regorafenib-MEK inhibitor combination (**Fig. 2a**) and having validated that prediction *in vitro* by demonstrating that regorafenib and MEK inhibitors exhibit the greatest synergy in D341 cells (**Fig. 2b**), we moved to investigate whether our findings would also hold *in vivo* (see **Methods**).

Given mirdametinib's superior brain penetration (compared to trametinib), as well as its greater synergy with regorafenib in the D341 cell line, we chose to advance the regorafenib-mirdametinib combination to *in vivo* testing (**Fig. 2b**). CD-1 nude mice orthotopically implanted with D341 cells were treated with regorafenib (10 mg/kg), mirdametinib (5 mg/kg), or their combination (**Fig. 3a**). Tumor progression was monitored weekly using IVIS imaging beginning one week post-implantation. The combination therapy surpassed the control and monotherapies in slowing tumor growth (**Fig. 3b** and **3c**), improving survival (**Fig. 3d**), and elevating apoptotic cell percentages (**Fig. 3e**).

To assess the generalizability of this approach, we also tested the *in vivo* efficacy of the mono- and combination therapies in the SHH model DAOY (**Fig. 3a** and **Supplementary Fig. 5a**). Unlike the aggressive D341 model, the DAOY model exhibited a longer median survival of 90 days in

the control group, compared to 34 days in D341. However, neither the single drug nor combination treatments provided significant survival benefits in the DAOY model (**Supplementary Fig. 5a** and **5b**), underscoring the specificity of this therapeutic strategy for G3 MB.

Recognizing the limitations of cell lines in fully recapitulating tumor biology, we extended our investigation to MB patient-derived xenografts (PDXs)[58, 59]. G3 MB PDXs produced significantly higher driver pair activity and drug sensitivity scores than normal cerebellum samples. Among the PDX models, PDX5950 was predicted to be the most sensitive (**Fig. 4a**). Mice orthotopically implanted with the PDX5950 model were treated with regorafenib and a reduced dose of mirdametinib (0.5 mg/kg) due to the model's increased MEK inhibitor sensitivity (**Fig. 4b**). Tumor progression was monitored weekly by MRI. As with the D341 model, combination therapy significantly reduced tumor burden in the PDX5950 model (**Fig. 4d**) and substantially extended survival (**Fig. 4c**). Mice treated with combination therapy had a median survival of 69 days, compared to 55, 55, and 59 days for mice treated with vehicle, mirdametinib, or regorafenib, respectively. We also found elevated apoptotic cell percentages in the combination therapy to a greater degree than the controls and monotherapies (**Fig. 4e**).

Body weight loss was noted in the D341-implanted mice three weeks post-implantation regardless of whether they received monotherapy, combination therapy, or vehicle control (**Supplementary Fig. 5c**). Blood analyses showed no significant differences across treatment groups, with all parameters except white blood cell (WBC) count remaining in the normal reference (**Supplementary Fig. 5d**). These findings suggest that weight loss was tumor-burden-related rather than treatment-induced. Mice implanted with PDX5950 experienced slight weight gain during the treatment window, reflecting the less aggressive nature of that model. Blood analyses similarly showed no significant differences across treatment groups, though the WBC counts of mice in the single-treatment arms fell outside the normal range. Notably, WBC count in the

combination group remained within normal limits, suggesting a potential protective effect of the combination therapy (**Supplementary Fig. 5e and 5f**).

Regorafenib plus MEK inhibitor enhances low-dose radiation therapy *in vivo*

Radiotherapy remains a cornerstone of medulloblastoma treatment[60], yet patients with G3 MB frequently experience tumor progression and poor survival outcomes[4, 6, 7, 61]. To investigate whether regorafenib and MEK inhibitors could enhance the efficacy of radiotherapy, we tested them in combination with low-dose irradiation using the D341 model. Mice were assigned to four treatment groups: vehicle control, drug combination alone, drug combination administered concurrently with radiation, and drug combination administered following radiation (**Supplementary Fig. 6a**). Radiotherapy was delivered in fractions of 0.5 Gy per day for five consecutive days. All treatment arms demonstrated improved survival compared to vehicle controls, with sequential therapy providing the greatest benefit over radiation alone (**Supplementary Fig. 6b and 6c**). Importantly, treatment-related toxicity (measured through body weight and blood analyses) was not observed in any of the experimental groups (**Supplementary Fig. 6d and 6e**).

These findings suggest that integrating regorafenib-MEK inhibitor combination therapy into existing treatment protocols may offer substantial therapeutic advantages for high-risk G3 MB patients, potentially improving outcomes for this challenging and aggressive subgroup of medulloblastoma.

Single-cell analysis reveals that regorafenib and MEK inhibitors target the developmental origins of G3 MB

Recent single-cell studies of human medulloblastoma have demonstrated significant intra- and inter-tumoral heterogeneity and diverse developmental origins of MB subtypes[62, 63, 64, 65, 66, 67]. To

understand how regorafenib-MEK inhibitor combinations affect different cell subpopulations in heterogeneous G3 MB, we analyzed drug target activity using single-cell RNA sequencing (scRNA-seq) data from human developing cerebellum, MB patient tumor samples, and the D341 xenograft model (both with and without treatment).

To investigate the developmental origins of each MB subtype, we used publicly available scRNA-seq data[66] to construct a developmental reference for human cerebellum, focusing on the glutamatergic lineage in which most MB occur. Our clustering analysis identified seven distinct developmental states based on previously published markers[68, 69, 70]: neural stem cells (NSC), rhombic lip progenitors (RL_pro), unipolar brush cell and granule cell precursor common progenitors (UBC_GCP_pro), unipolar brush cell progenitors (UBC_pro), granule cells (GC), and unipolar brush cells (UBC) (**Fig. 5a and 5b**; **Supplementary Table 7**). Pseudotime analysis with Slingshot and Monocle 3 produced a putative developmental trajectory in which NSCs progress along a single path to RL_pro and subsequently UBC_GCP_pro, at which point the trajectory bifurcates, ultimately giving rise to the UBC and GC lineages **(Supplementary Fig. 7a and 7b**; see **Methods**). This single-cell reference for human glutamatergic development is available via an interactive web portal (https://scminer.stjude.org/study/Glutamatergic-lineage).

Next, we performed clustering analysis of published MB patient scRNA-seq data[62, 63, 66] (**Supplementary Table 8**), and then used our developmental reference to assign developmental stages to each cluster. To do so, we extracted the malignant MB cells from the GSE155446 dataset (10,537 cells from one WNT, nine SHH, and 18 G3/G4 MB patients; **Supplementary Fig. 7c** and **7d**; **Supplementary Table 9**), annotating the clusters using marker genes for the seven developmental stages of the glutamatergic lineage (**Fig. 5c and Supplementary Fig. 7e**). Our mapped results revealed a predominance of GCP-like cells in SHH tumors, UBC_pro and UBC_GCP_pro cells in G3 tumors, UBC-like cells in G4 tumors, and RL_pro-like cells in WNT

tumors. Notably, the UBC_GCP_pro cluster closely resembled the NSC-like cells reported in the original study (**Supplementary Fig. 7d and 7e**). These findings, which suggest potential developmental origins for each MB subtype (**Fig. 5d**), were later validated using two independent scRNA-seq datasets[62, 66] (**Supplementary Fig. 7f-i**; **Supplementary Table 10-11**). The analyzed GSE155446 data, including gene expression and activity profiles, are available through an interactive portal (https://scminer.stjude.org/study/GSE155446).

In addition to the scRNA-seq analysis, we also employed our recently developed ReDeconv[71] algorithm to deconvolute bulk RNA-seq data from MB patient cohorts and PDX models (see **Methods**). Analysis of the mean percentage of each developmental state among patients with the same tumor subtype[9, 58, 72] revealed the same patterns observed in the scRNA-seq data (**Supplementary Fig. 8a**): SHH tumors were enriched with GCP-like cells, G3 tumors with UBC_pro and UBC_GCP_pro cells, and G4 tumors with UBC-like cells.

Next, we investigated the activity of BRAF and MAPK11, the primary targets of MEK inhibitors and regorafenib in G3 MB, across lineage stages. Using our scMINER algorithm[73] and the Mbi, we calculated driver activity at the single-cell level, revealing an elevation in the paired activity of BRAF and MAPK11 in the UBC_GCP_pro and UBC_pro-like subpopulations that are predominant in G3 tumors. No such elevation was observed for G3 minority subpopulations like GC and UBC, which represent more differentiated developmental states (**Fig. 5e**). The drug signature scores for regorafenib + MEK inhibitor showed a similar pattern of elevation in UBC_GCP_pro and UBC_pro-like cells. In contrast, both BRAF and MAPK11 activity and the drug signature scores were minimal in those patients' normal immune cells. Notably, expression of BRAF and MAPK11 was low across all malignant cell types, demonstrating the usefulness of the activity-based approach (**Supplementary Fig. 8b, 8c and 8d**). As expected, the drug signature scores were low in normal human cerebellum. BRAF and MAPK11 expression were

also low in normal cerebellum; however, BRAF+MAPK11 *activity* was markedly elevated in those samples' UBC_GCP_pro cells (**Supplementary Fig. 8e and 8f**).

These findings led us to hypothesize that regorafenib-MEK inhibitor combinations target the potential developmental origins of G3 MB, namely UBC_GCP_pro and UBC_pro cells. To test this hypothesis, we performed scRNA-seq profiling of D341 cells both prior to implantation in mice and then after implantation and treatment with vehicle control, mirdametinib, regorafenib, or their combination. Analysis of the pre-implantation D341 cells revealed high proportions of UBC_GCP_pro and UBC_pro-like subpopulations, much like the G3 MB patient samples (**Supplementary Fig. 8g and 8h**). D341 lacked mature-like populations (GC and UBC) and exhibited slightly higher proportions of GCP-like cells, likely due to culture conditions favoring proliferative progenitor-like states. The combined driver activity and drug signature scores were again exceptionally high in the UBC_GCP_pro-like tumor cells (**Supplementary Fig. 8i**).

Consistent with our findings *in vitro*, D341 tumor cells extracted from the mice post-treatment consisted primarily of UBC_GCP_pro and UBC_pro-like cells (**Fig. 5f and 5g**; **Supplementary Table 12**). There was a reduction in driver activity in the cells from the MIR and MIR+REG groups. Furthermore, the drug signature score was significantly lower in the MIR+REG group than in the vehicle control or single-agent group (**Fig. 5h and 5i**). The treatment effect was specific to cell state. The UBC_GCP_pro-like population demonstrated higher baseline driver activity and was more sensitive to treatment, leading to a decreased UBC_GCP_pro-to-UBC_pro cell ratio in the MIR and MIR+REG groups (**Fig. 5g and 5j**). The appearance of drug-resistant NSC-like tumor cells in the combination treatment group could be a source of treatment resistance.

Our single-cell analyses traced the major cellular origins of G3 MB to UBC_GCP_pro and UBC_pro cells in the glutamatergic lineage of developing cerebellum. Single-cell analysis of G3

MB cells treated *in vivo* confirm that UBC_GCP_pro and UBC_pro-like cells have greater driver activity and drug signature scores than other G3 MB tumor cell subpopulations; and that combination treatment is more effective than monotherapy and control at eliminating these tumor cells but may give rise to resistant populations.

Regorafenib plus MEK inhibitor is effective and reprograms the suppressive TME in an immunocompetent syngeneic mouse model of G3 MB

While our *in vivo* studies of human cell line xenografts (D341) and PDX models (PDX5950) were effective in establishing the efficacy of regorafenib-MEK inhibitor combinations in G3 MB tumors, these models require immune-deficient CD-1 nude mice, making them unsuitable for investigating drug treatment in the context of the tumor immune microenvironment. We therefore utilized CTD, a syngeneic G3 MB mouse model[74], to assess these combinations' efficacy in an immunocompetent setting and their impact on the TME.

CTD is a genetically engineered mouse model that resembles human G3 MB both histologically and molecularly[74]. In the CTD model, *Ctdnep1,* one of the most frequently altered tumor suppressors in G3 MB, is conditionally knocked out in neuronal progenitor cells or cerebellar stem cells, leading to MYC amplification and p53 inactivation, both hallmarks of G3 MB[74]. To confirm the faithfulness of the model, we used scRNA-seq to characterize cultured CTD tumor cells. Most of the CTD tumor cells were UBC_GCP_pro and UBC_pro-like, recapitulating the developmental origins of G3 MB (**Supplementary Fig. 9a**). Consistent with our findings in human G3 MB, the UBC_GCP_pro and UBC_pro-like cells had higher BRAF and MAPK11 activity and drug signature scores than RL_pro-like cells (**Supplementary Fig. 9b**). These results suggested that the CTD model was suited to our needs.

First, we tested the drug combination's efficacy and synergy in CTD cells *in vitro*. Similar to in the human PDX5950 model (**Fig. 4b**), the CTD mouse line exhibited notable sensitivity to MEK inhibitors. Adding even a low dose of MEK inhibitor significantly lowered the EC_{50} of regorafenib (**Fig. 6a and 6b**). Consistent with what was observed in human G3 MB cell lines (**Fig. 2e**), combination therapy simultaneously downregulated phosphorylated MEK (p-MEK), p-ERK, p-p38, and p-BRAF, while total protein levels remained unchanged (**Fig. 6c**).

We then evaluated the therapeutic efficacy of this combination *in vivo* using CTD-bearing C57BL/6 mice (**Fig. 6d**). Mirdametinib, selected for its high brain penetration, was administered at a low dose of 0.5 mg/kg given the high sensitivity of CTD to MEK inhibitors *in vitro*. Tumor volume was monitored via MRI weekly, and the relative tumor burden assessed four weeks post-surgery. Only the combination treatment group demonstrated a significant reduction in tumor burden compared to control (**Fig. 6e**). Combination treatment likewise significantly extended overall survival compared to monotherapy and control (**Fig. 6f**).

To investigate the effect of combination therapy on tumor cell states and the microenvironment, we performed scRNA-seq of endpoint tumor samples from each therapy group. To increase TME cell signal, we used CD45 antibody sorting to enrich the samples in immune TME cells, aiming for an equal ratio of $CD45^+$ and $CD45^-$ cells (**Fig. 7a**). scRNA-seq captured a total of 39,658 cells, including both tumor cells and a variety of TME cell types: macrophages, monocytes, microglia, dendritic cells, T cells, natural killer cells, neutrophils, basophils, endothelial cells, and oligodendrocyte progenitor cells (**Fig. 7b and Supplementary Fig. 9c**)

CTD tumors treated with regorafenib, both alone and in combination with mirdametinib, had a lower proportion of UBC_GCP_pro-like and UBC_pro-like tumor cells and a higher proportion of RL-pro-like cells compared to control and mirdametinib alone (**Fig. 7c and 7d**). Tumor cells

510 treated with REG and REG + MIR also showed reduced driver activity and drug signature scores
511 overall (**Supplementary Fig. 9d**). Not surprisingly, RL-pro-like tumors have lower drug signature
512 scores and driver activity compared to the drug-sensitive UBC_GCP_pro and UBC_pro-like
513 tumors (**Supplementary Fig. 9e**). Altogether, these data suggest that treating CTD tumors with
514 REG or REG + MIR reduces populations of drug-sensitive UBC_GCP_pro-like and UBC_pro-like
515 cells and increases populations of drug-tolerant RL-pro-like cells, producing the lower overall
516 driver activity and drug signature scores observed in these treatment groups.
517
518 To investigate whether drug treatment impacts tumor cells in other ways, we performed differential
519 expressed gene (DEG) analysis on the scRNA-seq data generated for our treatment groups.
520 Tumor cells treated with combination therapy showed up-regulation of MHC complex genes (*H2-*
521 *D1*, *H2-K1, H2-Aa, H2-Ab1, B2m* and *H2-Eb1*) and downregulation of *Lgals3*, a ligand of LAG3,
522 an immune checkpoint receptor expressed on T cells[75] (**Fig. 7e**). The function enrichment analysis
523 show the upregulated DE genes (avg_log2FC > 1, adjusted p value < 0.05) are related to tumor
524 antigen presentation[76] (**Fig. 7f**). We summarized antigen presentation related genes into a
525 module score and found across all treatment groups, with combination therapy producing the
526 highest score (**Fig. 7g and Supplementary Fig. 9f**).
527
528 Next, we used the scRNA-seq data to compare the immune cell type proportions of our treatment
529 groups (**Supplementary Table 13**). Sixteen immune cell types were captured, including seven T
530 cell populations (**Fig. 7b and 7h**). Monocytes (Mono) and T effector cells (Teffector) were
531 increased, and T regulatory cells (Treg) were decreased, in the combination therapy group
532 compared to control and monotherapy (**Fig. 7h and 7i**). Notably, the combination therapy group
533 had increased macrophages (**Fig. 7i**), but a greater proportion of those were of the M1 phenotype
534 (**Supplementary Fig. 9g**; **Supplementary Table 14**), consistent with a previous report that
535 regorafenib enhances M1/M2 polarization in head and neck cancers[77]. In terms of T cells, we

found a reduction in immunosuppressive Tregs and an increase in CD8+ T effector cells in the combination therapy group (**Fig. 7i**); in fact, this group had the highest ratio of CD8+ T effector cells to Tregs (**Fig. 7j**), indicating more robust anti-tumor immunity compared to the other groups. This owes to the increased antigen presentation previously observed in tumor cells.

Then to understand how the drugs changed TME globally, we calculated drug scores for immune cells. Immune cells in the combination therapy group scored highest for MIR and REG, indicating that these treatments may alter the transcriptomes of immune cells (**Supplementary Fig. 10a**, see **Methods**). Tregs had the highest scores for both drugs; T effector cells and monocytes also presented high scores (**Supplementary Fig. 10b**). These results suggest that drug treatment may directly shape the cell type composition of the TME.

We also found that CD8+ T cells (Tex, T effector cells, Tcm and proliferative T cells) were more activated, as indicated by increased expression of *Ifng*, *Prf1*, in the combination treatment group (**Supplementary Fig. 10c**). These T cells also expressed more *Ccl3* and *Ccl4*, which have been shown to increase T cell activation[78, 79]. CCL3 and CCL4 secretion has also been reported in T effector cells activated by infections[80]. CD8+ T cells in the combination therapy group also showed upregulation of *Cxcr6* and downregulation of *Cxcr4*. *Cxcr6* has been noted to promote T cell activation and recruit T cells into tumors, while *Cxcr4* mainly mediates the exclusion of T cells from the tumor center. Collectively, these evidence suggest that combination treatment could promote CD8+ T cells anti-tumor immunity[81, 82, 83,84]. CD8+ T cells in the combination treatment group also showed increased expression of several immune checkpoints and immunotherapy targets[85, 86], including PD1, LAG3, TIM3, CD160, and CD39 (**Supplementary Fig. 10c and d**), indicative of CD8+ T cell exhaustion—a potential source of the resistance observed in this treatment group. Supplementing regorafenib + MEK inhibitors with immunotherapy may therefore

561 achieve better efficacy in clinical settings and is a strategy worth exploring (**Supplementary Fig.**
562 **10e**).
563
564 Previous studies have shown that besides direct activation by TCR, expression of CCL3 and
565 CCL4 in T cells can also be induced by IL12, IL18 and IFNg[80, 87]. Among the cell types captured
566 in the TME, monocytes exhibited the greatest expression of *Il18*, while its receptors (*Il18r* and
567 *Il18rap*) were highly expressed on T cells (**Supplementary Fig. 10f-10i**). Given the higher
568 proportion of monocytes in the combination therapy group, the increased T cell activation
569 observed in this group could be explained by increased secretion of CCL3 and CCL4 in CD8+ T
570 cells induced by monocyte-derived IL18 (**Supplementary Fig. 10j and 10k**). This explanation
571 was partially supported by CellChat analysis[88] of ligand-receptor interactions on the IL18-IL18R
572 and CCL3/4-CCR5 axis. T effector cells in the combination therapy group received more
573 communications from IL18 (**Fig. 7k**, see **Methods**). However, no trend was observed in the IL18
574 communications received by immune-suppressive Tregs. For the CCL3/4-CCR5 axis, we found
575 an increase in communications received by T effector cells in both the mono- and combination
576 therapy groups, with communication levels greatest in the latter. Notably, MIR treatment blocked
577 CCL3/4-CCR5 communications received by Tregs. Together, these data demonstrate
578 combination therapy-induced activation of the CCL3/4-CCR5 axis in T effector cells but not
579 immunosuppressive Tregs, potentially explaining the greater active antitumoral immunity in the
580 combination therapy group.
581
582 In summary, regorafenib and MEK inhibitors not only demonstrated robust anti-tumor efficacy in
583 a syngeneic mouse model of G3 MB, but also triggered anti-tumor immunity through the activation
584 of cytotoxic CD8+ T cells, suggesting the combination's promise for overcoming tumor
585 progression and immune evasion in the clinic.
586

DISCUSSION

To our knowledge, this study is the first to use systems biology approaches to guide high-throughput combination drug screening in high-risk medulloblastoma. The SINBA platform brings together gene activity data, a brain-penetrating drug database, and single-agent high-throughput screening results to nominate synergistic drug pairs for combination screening. Through single-agent screening, we identified both novel and previously reported G3 MB-specific drugs, such as mycophenolate mofetil and digoxin[89]. Applied to transcriptomic data from three MB patient cohorts, SINBA predicted a regorafenib-MEK inhibitor combination for G3 MB; these drugs were later confirmed to be synergistic both *in vitro* (through drug screening) and *in vivo* (through efficacy studies). We found that tumor cells sensitive to the regorafenib-MEK inhibitor combinations share transcriptomic signatures with early unipolar brush cell (UBC) progenitors, which have previously been proposed as the cell-of-origin for G3 MB[62, 64, 65, 90, 91]. We also showed that a regorafenib-MEK inhibitor combination reprograms the tumor microenvironment, enhancing CD8+ T cell recruitment in an immunocompetent G3 MB mouse model.

G3 medulloblastoma is an aggressive cerebellar tumor arising from malignantly transformed early UBC progenitors within the rhombic lip subventricular zone (RL^{svz})[64, 65, 91]. Single-cell analyses comparing MB cells to normal cerebellar references have found that MB cells arise from early developmental arrest[92] driven by genetic mutations or epigenetic dysregulation[64,9, 93]. Novel immunotherapies, such as CAR-T cells targeting Protogenin-expressing stem cells, have shown efficacy in preclinical G3 MB models in immunocompromised mice[91]. However, drug repurposing strategies that target origin cell populations *in vivo* are lacking. While SINBA is not expressly designed to select drugs that target originating populations, it may nonetheless propose drug pairs that do so, as it did for G3 MB.

Robust clinical and preclinical evidence suggest that combining regorafenib with MEK inhibitors may effectively treat brain tumors[94, 95, 96, 97]. In the phase II REGOMA trial, treating relapsed glioblastoma patients with regorafenib produced better therapeutic outcomes than lomustine[28]. The MEK inhibitor trametinib, in combination with the BRAF inhibitor dabrafenib, received FDA approval in 2022 for the treatment of advanced tumors with BRAF V600E mutations, including adult and pediatric gliomas. Another MEK inhibitor, mirdametinib, recently gained FDA approval for treating plexiform neurofibromas in both adult and pediatric populations. Notably, combining mirdametinib with the PI3K/mTOR inhibitor paxalisib significantly extends survival in mouse models of pediatric high-grade gliomas[53]. Given its more favorable pharmacokinetics and CNS activity, mirdametinib replaced trametinib as the MEK inhibitor in our experiments *in vivo*.

Through the SINBA algorithm, trametinib and regorafenib were identified as a potentially synergistic drug combination that targets BRAF and MAPK11 (a p38 subunit), hidden drivers in G3 MB. Although this drug combination has not previously been tested in MB, MEK inhibitors and regorafenib have demonstrated synergistic effects in colorectal cancer[98, 99], gastric cancer[100] and melanoma models harboring BRAF V600E mutations[101]. While BRAF mutations are rare in MB, upregulation of MEK kinase activity—a downstream target of BRAF—is common, even in the absence of changes to the total protein levels[47]. Overexpression of the PDGFA/RAS/MAPK signaling pathway has been implicated in MB metastasis[102, 103], and inhibition of MEK1/2 with U0126 has been shown to reduce viability in MB[104]. Additionally, treatment-resistant MB cells maintain a stem cell-like state through overexpression of the BPIFB4 (bactericidal/permeability-increasing fold-containing family B member 4) longevity factor. Reducing BPIFB4 levels in recurrent MB cells diminishes their aggressiveness both *in vitro* and *in vivo*, with the ERK1/2 and p38α proteins most affected by BPIFB4 knockdown[105]. These findings align with previous studies demonstrating that targeting ERK (a downstream target of MEK) and p38-MAPK signaling with liposomal honokiol induces ROS-mediated apoptosis in MB cell line models[106].

The regorafenib-MEK inhibitor combination inhibits cancer progression both directly, by targeting cancer-driving genes, and indirectly, through modulation of the TME. MEK inhibition protects tumor-infiltrating CD8+ T cells from exhaustion driven by chronic TCR stimulation while preserving cytotoxic activity[107]. Regorafenib promotes a tumor suppressive microenvironment by promoting Macrophage M1/M2 polarization and by decreasing expression of PD-L1 and increasing expression of MHC-I class genes in tumor cells[77, 108, 109]. These observations are consistent with our finding that regorafenib-MEK inhibitor therapy promotes an antitumor TME in G3 MB. Combination therapy-induced up-regulation of CD8+ T cell immunotherapy targets could explain the resistance observed, as well as offer a potential solution: adding an immune checkpoint blockade, such as PD-L1/PD1, LAG3, or TIM3. At present, no immunotherapy has been approved for G3 MB tumors, which are typically immunotherapy-resistant and considered immunologically "cold". Adjunctive regorafenib-MEK inhibitor therapy could sensitize these tumors to immunotherapy, providing a path forward for that treatment modality in G3 MB.

This study establishes SINBA as a powerful tool for uncovering synergistic drug combinations that target critical hidden drivers in high-risk MB and beyond. A regorafenib + MEK inhibitor combination based on SINBA's predictions was found to disrupt key oncogenic pathways and actively reprogram the TME towards an anti-tumor state, presenting a compelling therapeutic strategy for G3 MB. Future directions include further refinement of SINBA's drug-target database as well as translational investigations aimed at bringing the regorafenib + MEK inhibitor combination into clinical use. Further studies should evaluate the combination as an adjunct to standard chemotherapy, radiation, and immune checkpoint inhibitors, particularly the latter given MB's immune-cold nature and the combination's TME-modulatory effects. To maximize efficacy and address potential resistance, investigations should also be made into this combination's impact on tumor cell plasticity and dynamic immune system interactions.

MEHTODS

Chemicals

Regorafenib monohydrate (HY-10331A), Trametinib (HY-10999), and Mirdametinib (PD0325901, HY-10254) were obtained from MedChemExpress (MCE). For in vitro studies, each compound was dissolved in dimethyl sulfoxide (DMSO; FisherScientific, BP231-100) to a final stock concentration of 10 mM. For in vivo preclinical studies, the compounds were formulated as follows. 1. Regorafenib: The free base equivalent of regorafenib was calculated using a correction factor of 1.0373 for its monohydrate form. The drug was first dissolved in an 80% non-aqueous vehicle consisting of propylene glycol (PG, 42.5%), polyethylene glycol 400 (PEG400, 42.5%), and Pluronic F68 (15%) (v/v/v) by heating to 60 °C with agitation and vortexing. The solution was then brought to final volume with ultra-pure water at room temperature, yielding a clear formulation for oral gavage at a concentration of 3 mg/mL, administered at 10 mL/kg. 2. Trametinib: A 3 mg/mL stock solution was prepared in DMSO. For oral administration, the stock was diluted to 1% DMSO in a vehicle consisting of 10% Cremophor RH40, 10% PEG400, and 80% ultra-pure water, resulting in a final dose concentration of 0.03 mg/mL, delivered at 10 mL/kg. 3. Mirdametinib: The compound was formulated at 2.5 mg/mL in an aqueous suspension containing 1% methylcellulose and 1% Tween 80. The formulation was prepared using sonication to ensure uniform dispersion and administered by oral gavage at a dose volume of 10 mL/kg.

The SINBA algorithm to identify synergistic drug pairs for G3 MB

The SINBA package is available on GitHub with a detailed tutorial (https://github.com/jyyulab/SINBA). Below, we outline the steps used to identify synergistic therapeutics for Group 3 medulloblastoma (G3 MB) using SINBA.

1. Construction of medulloblastoma-specific gene-gene interaction network

To reconstruct medulloblastoma-specific interactomes (MBi), we applied the SJARACNe algorithm[41, 110] to a curated microarray dataset, DKFZ_SJ, comprising 407 medulloblastoma patient samples. Using Gene Ontology classifications, we compiled a list of 11,239 transcription factor (TF) genes and signaling molecules to serve as hub genes in the MBi. Separate transcription factor (TF) and signaling molecule (SIG) networks were generated using SJARACNe. In this final network, drivers were linked to their downstream targets through edges based on gene–gene mutual information derived from their expression patterns. The reconstructed MBi consisted of 38,621 probe nodes and 1,567,381 interactions, representing 12,495 hub probes (corresponding to 7,155 genes) and their downstream target probes.

2. Identification of G3-Specific Drivers

Hub gene activities for each sample in the DKFZ_SJ dataset (407 MB patients, 4 normal cerebellum) were inferred using NetBID2 package[45] function **cal.Activity** (es.method = "weightedmean"), which integrates gene expression profiles with the MBi. G3-specific drivers were selected based on the following criteria, resulting in 75 candidates:

- Adjusted p-value for G3 vs. other subgroups < 1e-5, with Z-score > 0.
- Adjusted p-value for G3 vs. normal cerebellum < 1e-3, with Z-score > 0.
- Regulon size between 50 and 500.

3. Refinement of G3-Specific Drivers

To refine the list, we used SINBA's built-in Brain Penetrant database (BPdb) to filter for druggable drivers, yielding 45 seed drivers targeted by 69 compounds. TF and SIG networks were merged using the SINBA function **get.combined.network** to prepare for activity calculations and driver-pair predictions. Driver pairs were generated either manually or by unbiasedly combining seed drivers with all druggable hub genes using the **combineNet2Target_list** function.

Following seed drug library screening, 20 drugs (targeting 20 seed drivers) with EC20 < 10 μM or the solo agent targeting on the interesting seed drivers.

4. Prediction of Driver Pairs and Drug Pairs

Driver-pair predictions were performed by combining the TF and SIG networks and pairing the 20 seed drivers with all druggable MBi hub genes using the **combineNet2Target_list** function. Activities for single drivers and driver pairs were calculated using **cal.SINBA.Activity**. Driver pairs were ranked using **get.SINBA.DE.2G**, which computes statistical values comparing G3 with other subtypes and normalizes p-values into Z scores (Z.pair). Z scores for seed (Z.seed) and partner drivers (Z.partner) were calculated similarly. The delta.Z score was defined as:

$$\text{delta.Z} = \frac{\text{Z.pair(G3.vs.other subtype)}}{\sqrt{2}} - \frac{\text{Z.seed(G3.vs.other subtype)} + \text{Z.partner(G3.vs.other subtype)}}{2}$$

A genetic algorithm[111] (implemented in the function **find_max_sum_submatrix**) was then employed to optimize the maximum sum of delta.Z scores (*in silicon* synergistic scores) for G3 vs. other subtypes. The final matrix layout consisted of 20 seed drivers × 16 partner drivers. BPdb was then used to convert driver pairs into drug pairs.

SINBA-guided drug combination screening

1. Single-Drug Dose–Response Testing

A total of 90 compounds (69 predicted seed drugs and 21 partner drugs) identified by the SINBA algorithm were screened. Compounds were tested in 10-point dose-response curves (10 μM to 0.47 nM, 1:3 serial dilution) against the HDMB03 cell line. Cell culture conditions, tumor

dissociation protocols, and density optimization followed established methods[112]. HDMB03 cells were seeded in 384-well plates. After 24 hours, compounds were pin-transferred (Biomek FX Workstation; Beckman Coulter) with negative (0.08% DMSO) and positive control (1.6 μM staurosporine; MedChemExpress, HY-15141). Cell viability was assessed 7 days post-treatment using CellTiter-Glo® (Promega, G7572). Dose-response curves were fitted using the drc package[113] with four-parameter log-logistic function to estimate EC_{20}, EC_{50} values, which defined low- and high-dose conditions (with fixed defaults of 1 μM and 6 μM, respectively, for drugs lacking EC_{20} or EC_{50} values).The four-parameter log-logistic function is given by the expression:

$$f(x) = c + \frac{d - c}{1 + \exp\left(b(\log(x) - \log(e))\right)}$$

2. Two-dose combination testing

To prioritize the drug pairs testing for synergy, 320 SINBA-predicted drug pairs were tested in 384-well plates (64 wells reserved for controls). Each pair included four conditions: drug1 low dose+ drug2 high dose; drug1 high dose + drug2 high dose; drug1 low dose + drug2 low dose; drug1 high dose + drug2 low dose. 7 days after treatment, viability was measured (CellTiter-Glo®, Promega) and normalized to controls. Combination effects were quantified as:

$$Combo_{effect} = Ecombo - \frac{Edrug1 + Edrug2}{2}$$

3. 10-dose combination screening

32 prioritized pairs were tested in full dose-response matrices (10×10 concentrations, 10 umol/L to 0.14 nmol/L). Drugs were added simultaneously, and viability was assessed after 7 days.

764 Synergy score were calculated using the synergyFinder package[114] with zero interaction potency
765 (ZIP) model[32].
766
767 **Medulloblastoma Patient SINBA Shiny App**
768 We developed a medulloblastoma-specific SINBA Shiny app to provide a comprehensive
769 resource for exploring MB patient data(https://yulab-stjude.shinyapps.io/SINBA_MB). The app
770 includes pre-built MBi networks, curated six drug-gene interaction databases, driver and driver-
771 pair activity profiles, gene expression profiles, and patient clinical outcomes. Users can flexibly
772 select druggable drivers using six integrated drug-gene interaction databases and explore
773 potential synergistic driver pairs. This tool is designed to support hypothesis generation and
774 facilitate the identification of therapeutic targets in medulloblastoma research.
775
776 **Cell culture and transfection**
777 G3 MB human cell line HDMB03 and MB002 were generously provided by Dr. Till Milde and Dr.
778 Jae-Youn Cho, respectively[115, 116]. PDX model SJMBG3-12-5950 (PDX5950) was utilized as
779 described in the published work[58]. Human SHH subgroup DAOY cell line was purchased from
780 American Tissue Culture Collection (ATCC, HTB-186). Human G3 cell lines D341, D283, D425
781 and mouse model CTD[74] were generously provided by Dr. Richard Q. Lu. Human cell lines and
782 PDX model were cultured as neurospheres in supplemented neurobasal medium per established
783 protocol[117]. All lines underwent quarterly mycoplasma testing (MycoAlert™, Lonza) and
784 maintained <10 passages post-thaw.
785
786 To generate the luciferase-expressing D341 cell line, cells were infected with a lentiviral vector
787 (CL20SF2-Luc2aYFP) containing the firefly luciferase and yellow fluorescent protein (YFP) genes
788 at a multiplicity of infection (MOI) of 20. Following infection, cells were sorted based on YFP
789 fluorescence to select for positively transduced cells.

The mouse model CTD was cultured using previously published methods. Briefly, CTD cells were grown in DMEM/F-12 medium supplemented with HEPES buffer, sodium pyruvate, non-essential amino acids, GlutaMax (Thermofisher Cat# 35050061) and B-27 supplement (Thermofisher Cat# 17504044) at 37°C and 5% CO2. A total of $1x10^6$ CTD cells were infected with 1µl of virus (titer $4x10^{10}$) for 48h. Then YFP+ cells were sorted by fluorescent-activated cell sorting (FACS).

Drug signature score calculation in medulloblastoma tumors

Gene signatures induced by regorafenib and trametinib treatment in the central nervous system were obtained from the iLINCS database (https://www.ilincs.org/ilincs/;regorafenib: CTRS_2230; trametinib: CTRS_2295; Table S15). Differentially expressed genes were identified using cutoffs of |logFC| > 1.5 and p-value < 0.01. This analysis identified 103 upregulated and 42 downregulated genes following regorafenib treatment, and 32 upregulated and 28 downregulated genes following trametinib treatment. The upregulated and downregulated gene sets from both treatments were merged to represent the combined effects of the drug pair.

To calculate MEK inhibitor plus regorafenib signature scores in MB tumor cells, gene expression profiles were first converted to activity profiles by integrating the medulloblastoma-specific interactome (MBi) for bulk or single-cell RNA-seq samples. Activity profiles were standardized using z-transformation. Upregulated and downregulated gene sets were analyzed separately using the NetBID2 function **cal.Activity.GS** (es.method = "ssgsea"). For each sample, the drug pair signature score was calculated by subtracting the ssGSEA score of the upregulated gene set from that of the downregulated gene set, quantifying sensitivity to the combination treatment.

***Ex vivo* evaluation of MEK inhibitor and regorafenib combination efficacy by AlamarBlue assay**

The viability of D341, MB002, D283, D425, DAOY, SJMBG3-12-5950 (PDX5950), and CTD cells were assessed in the presence of MEK inhibitors (trametinib or mirdametinib/PD901) in combination with regorafenib using full dose-response matrices (10×10 concentrations, ranging from 10 umol/L to 1 nmol/L Drugs were transferred into 384-well plates using the Echo 650 series acoustic liquid handler for precise nanoliter-scale dispensing.

Cells were seeded into the drug-treated plates at a density of 1 × 10^3 cells per 30 µL of medium and incubated for seven days under standard culture conditions. After seven days, cell viability was measured using the AlamarBlue assay. Briefly, 10% AlamarBlue reagent was added to the cells in complete medium, and the plates were incubated for 1-4 hours according to the manufacturer's protocol. Absorbance was measured using a plate reader to quantify cell viability. The calculation of synergistic effects was performed as described in the SINBA-guided high-throughput screening section.

Drug treatment and western blot

Human G3 cell lines or mouse mode CTD cells were seeded into 6-well plates and treated with regorafenib, either alone or in combination with trametinib or mirdametinib, at the indicated concentrations. After 3 days of treatment(72 h), cells were harvested and lysed in RIPA buffer supplemented with protease and phosphatase inhibitors (#78440, Thermo Fisher Scientific) for 20 minutes. Total protein extracts were separated by SDS-PAGE and transferred onto polyvinylidene fluoride (PVDF) membranes (Millipore, USA) using the Trans-Blot Turbo™ transfer system (Bio-Rad, USA).

The PVDF membranes were blocked with 5% non-fat dry milk in TBS-T for 1 h at room temperature. Following blocking, the membranes were incubated overnight at 4°C with primary antibodies (Cell Signaling Technology). After washing three times with TBS-T, the membranes

were incubated with HRP-conjugated secondary antibodies (ABclonal) for 1 h at room temperature. Protein bands were visualized using an enhanced chemiluminescence (ECL) kit (ABclonal) and imaged with the Bio-Rad ChemiDoc MP Imaging System.

Pharmacokinetics of regorafenib, mirdametinib and trametinib in mice

The plasma and brain pharmacokinetic (PK) profile of regorafenib was evaluated in normal female Crl:CD1 (ICR) nude mice (7 to 11 weeks old; Charles River Laboratories, Stock Number 086). Regorafenib monohydrate (MedChem Express, CAT# HY-10331A, LOT# 09764) was suspended in 80% (propylene glycol 42.5% / polyethylene glycol 400 42.5% / Pluronic F68 15%) and 20% ultra-pure water (Millipore), at 1 mg/mL for a 10 mg/kg free base equivalent dose. Terminal samples, one from each mouse, were collected over a 24-hour post-dose period by cardiac puncture using a 1 mL syringe, the blood placed in a Sarstedt Microvette K3EDTA 500 µL tube and immediately separated to plasma. The carcass was then perfused with PBS, the brain extracted, rinsed, and placed in a microcentrifuge tube. All samples were immediately stored on dry ice and transferred to -80 °C until analysis. Remaining regorafenib dosing suspension was submitted for verification of potency, and chemical and physical stability during the study period.

For brain exposure studies of trametinib and mirdametinib, 10 mmol/L stock solutions were initially prepared in DMSO. These stocks were subsequently diluted to a final concentration of 1 mmol/L using a sequential dilution method with 30% polyethylene glycol 400 (PEG400) and 60% phosphate-buffered saline (PBS). Intravenous dosing was performed at 5 mL/kg. Samples were collected as regorafenib study.

Brain exposure was assessed by determining the unbound brain-to-plasma partition ratio ($K_{p,uu}$), a critical parameter in evaluating central nervous system (CNS) drug penetration and distribution. $K_{p,uu}$, derived from the total brain-to-plasma partition ratio (K_p), was calculated using Equation (1),

as previously described[51]. Unbound drug exposures were estimated based on measured total drug concentrations in plasma and brain, in combination with experimentally determined fractions unbound in plasma ($f_{u,plasma}$) and brain tissue ($f_{u,brain}$). Plasma and brain concentration-time data for the agents were summarized, with the mean values subjected to standard noncompartmental analysis (NCA) using Phoenix WinNonlin 8.1 (Certara USA, Inc., Princeton, NJ). The apparent plasma-to-brain partition coefficient (Kp) in mice was estimated as the ratio of the area under the concentration-time curve (AUC) in brain to the AUC in plasma.

$$K_{p,uu} = K_p \times \frac{f_{u,brain}}{f_{u,plasma}} = \frac{AUC_{brain} \times f_{u,brain}}{AUC_{plasma} \times f_{u,plasma}} \quad (1)$$

***In vivo* evaluation the efficacy of mirdametinib plus regorafenib**

Luciferase-positive D341 cells (30,000 cells/mouse), PDX5950 (SJMBG3-12-5950) tumor cells (500,000 cells/mouse), DAOY cells (500,000 cells/mouse) and luciferase-positive CTD cells (1,000,000 cells/mouse) were resuspended in 5 µL Matrigel (BD Biosciences, 356234) and stereotactically implanted into the cortices of 7–11-week-old female CD-1 nude mice or male C57BL/6J mice (for CTD models; The Jackson Laboratory, Cat. 000664). Tumor growth was monitored weekly using bioluminescence imaging (BLI) with a PerkinElmer IVIS system or magnetic resonance imaging (MRI), as previously described[112]. Treatment was initiated one week after implantation surgery. Mice were randomized into treatment groups and continuously dosed for six weeks with vehicle, mirdametinib, regorafenib, or the combination of mirdametinib and regorafenib. Regorafenib was administered at a fixed dose of 10 mg/kg across all models, while mirdametinib was dosed at 5 mg/kg for D341 and DAOY models and 0.5 mg/kg for PDX SJMBG3-12-5950 and CTD models. For combination therapy tested with D341 model, involving regorafenib

(10 mg/kg), mirdametinib (5 mg/kg), and irradiation, radiation was delivered using the Small Animal Radiation Research Platform (SARRP, Xstrahl Life Sciences). An 8 mmx 11 mm treatment field was delivered to the brain using opposed lateral beams 0.5 Gy/day for 5 days to a total dose of 2.5 Gy. Detailed irradiation protocols have been previously published[118].

Mice that reached the experimental endpoint were euthanized, and tumors were harvested and snap-frozen for molecular analysis. Mice were excluded from the study if they died prematurely, failed to develop tumors, or required humane euthanasia due to unrelated health conditions without tumor burden. All experiments were conducted in accordance with the National Institutes of Health's Guide for the Care and Use of Laboratory Animals and were approved by the St. Jude Children's Research Hospital (SJCRH) Institutional Animal Care and Use Committee (IACUC protocol #3078).

Toxicity was assessed weekly by measuring body weight and performing endpoint blood work. Complete blood counts were obtained from whole blood treated with ethylenediamine tetra-acetic acid (EDTA) using a Forcyte Hematology Analyzer (Oxford Scientific), which employs impedance and laser technology. Serum diagnostic chemistry panels were analyzed using the Trilogy chemistry analyzer (Drew Scientific).

Visualization Web Portal for Single-Cell Glutamatergic Lineage Developmental Reference and Medulloblastoma Patient Data

To facilitate data exploration and visualization, we developed two interactive web portals: one for the glutamatergic lineage reference (https://scminer.stjude.org/study/Glutamatergic-lineage) and one for medulloblastoma patient data (https://scminer.stjude.org/study/GSE155446). The portals were built with JavaScript and Vue.js for the frontend, Java and Spring Boot for the backend, and

Neo4j and MySQL databases for efficient data management. The web portal provides access to three main functionalities: dataset presentation, data visualization, and data downloading.

For glutamatergic lineage analysis, we curated a public scRNA-seq dataset of the human fetal cerebellum generated with the 10X Chromium platform[66]. From this dataset, glutamatergic lineage cells were filtered by selecting cell populations annotated as "01xNSC," "06xGCP_progenitor," "07xGCP_1," "08xGCP_2," "09xGranule_cell," "10xUBC_progenitor," "11xDiff.UBC," and "11xUBC" in the original study. To account for major sequencing batch effects, present in the dataset, UMAP-level batch correction was performed using Harmony prior to downstream clustering and visualization. Unsupervised Leiden clustering, combined with previous annotations and manual curation informed by known lineage markers, resulted in the identification of seven distinct glutamatergic lineage cell types: neural stem cells (NSC), rhombic lip progenitors (RL_pro), unipolar brush cell and granule cell precursor common progenitors (UBC_GCP_pro), unipolar brush cell progenitors (UBC_pro), granule cell precursors (GCP), granule cells (GC), and unipolar brush cells (UBC).

For medulloblastoma patient data, single-cell RNA-seq profiles from 28 pediatric tumors (1 WNT, 9 SHH, 7 Group 3, 11 Group 4; GEO accession GSE155446) were processed using the Seurat workflow, with batch correction via Harmony. Cell type annotations were adopted from the original publication or re-annotated using the glutamatergic lineage reference.

Both portals integrate single-cell expression profiles with the medulloblastoma-specific interactome (MBi), utilizing the scMINER algorithm[73] to generate activity profiles. Users can query both gene expression and activity profiles for any given list of driver genes. The portal supports various visualization tasks, including clustering UMAPs, heatmaps, bubble plots, violin plots, and

network plots, enabling users to explore lineage-specific patterns and driver activity in a user-friendly environment.

Pseudotime trajectory analysis for the glutamatergic lineage cells

The differentiation trajectory of glutamatergic lineage cells was reconstructed using Slingshot[119] (v2.10) and Monocle 3[120] (v1.3). The UMAP projection of glutamatergic lineage cells was imported from a Seurat object for downstream analysis. For pseudotime calculation with Slingshot, the slingshot function was applied to compute the arc length from the starting point (neural stem cells, NSC) to all projected points along the principal curve, assigning pseudotime values to each cell. To construct the trajectory with Monocle 3, sample-based batch effects were corrected using the align_cds function. The UMAP projection was imported from the Seurat object, and the differentiation trajectory was generated using the learn_graph function. NSC cells were selected as the starting point for the pseudotime trajectory. The trajectory, aligned with the UMAP projections, was visualized using the plot_cells function in Monocle 3.

Deconvolution of Glutamatergic Lineage Developmental States in Bulk RNA-seq Samples of MB Patients or PDOX

To prepare the dataset for deconvolution, we normalized the reference glutamatergic lineage single-cell counts to 1×10^6 and used the seven cell type annotations as input for ReDeconv package[71] built-in functions **get_initial_Signature_Candidates** and **Get_signature_gene_matrix**. The following parameters were applied:

- L_topNo = 200
- L_max_pv = 0.05
- L_min_fold_change = 2.0
- L_CellType_CellNo_LB = 30

- L_NoSep_sampleNo_UB = 2

After generating the glutamatergic lineage cell type signature gene matrix, we applied the **ReDeconv** function to deconvolute glutamatergic lineage developmental state proportions in bulk RNA-seq samples from public medulloblastoma patient datasets and patient-derived orthotopic xenograft (PDOX) bulk RNA-seq data, which were quantified as FPKM. The seven cell type signature matrix served as input for this deconvolution process, allowing us to estimate the relative proportions of developmental states in each bulk RNA-seq sample.

Single-cell RNA-seq profiling of human cell line D341 and mouse model CTD *in vitro*

Cells from either the mouse syngeneic G3 MB model (CTD) or the human G3 MB cell line (D341) were dissociated with Accutase (Stemcell Technologies, Cat# 07922) at 37°C for 5 minutes. Then we input 8000 cells with 80% viability to the workflow of 3' gene expression of 10x genomics. The 10x Genomics Chromium controller instrument was used for Gel Bead-in-Emulsion (GEMs) preparation. Gel Bead-in-Emulsion (GEM) generation was performed using the Chromium Controller, followed by single-cell library preparation using Chromium Next GEM Single Cell 3′ Kit v3.1 (PN-1000269), Chromium Next GEM Chip G Single Cell Kit (PN-1000127) and Dual Index Kit TT Set A (PN-1000215). cDNA and final barcoded sequencing libraries were constructed following the manufacturer's guidelines and subsequently assessed for quality and concentration using Tapestation.

Single-cell RNA-seq profiling of human model and mouse model after treatment in preclinical study

In vivo-implanted D341 mouse tumors were harvested at the endpoint. Tumor tissues were minced and digested at 37°C for 30 minutes using the Human Tumor Dissociation Kit (Miltenyi Biotec, catalog no. 30-095-929). Red blood cells were removed by treatment with ACK lysis buffer

(Thermo Fisher Scientific, catalog no. A1049201). The digested tissues were then passed through a 70 μm cell strainer to obtain a single-cell suspension. Approximately 8,000 cells with over 80% viability were selected and processed using the Flex Gene Expression workflow from 10x Genomics for downstream analysis.

Mouse CTD tumors were harvested at end point. Mouse tissues were minced and digested at 37°C for 1 h (1mg/mL papain, 10 μg/mL DNase I, 10% heat-inactivated FBS in RPMI) to dissociate cells. Red blood cells were lysed with ACK lysis buffer (Thermo Fisher Scientific, catalog no. A1049201). Then tissues were passed through 70 μm cell strainer to get single-cell suspension. Then cells were incubated with CD16/32 antibody (Miltenyi Biotec, Cat#130-092-575) for 20 minutes on ice to block Fc receptors. Next, they were stained with PE-CD45 antibody (Biolegend, Cat# 157603) on ice for 20 minutes and DAPI (1ug/ml) on ice for 3 minutes. Then live immune cells (CD45+) and tumor cells (YFP+) were sorted by FACS and combined for downstream library preparations.

Then we input 8000 cells with 80% viability to the workflow of Flex gene expression of 10x genomics. The 10x Genomics Chromium controller instrument was used for Gel Bead-in-Emulsion (GEMs) preparation. Gel Bead-in-Emulsion (GEM) generation was performed using the Chromium Controller, followed by single-cell library preparation using GEM-X Flex Sample Preparation v2 Kit (PN-1000781), GEM-X Flex Gene Expression Chip Kit (PN-1000791), GEM-X Flex Gene Expression Mouse Transcriptome probe kit (PN-1000786) and Dual Index Kit TT Set A (PN-1000215). cDNA and final barcoded sequencing libraries were constructed following the manufacturer's guidelines and subsequently assessed for quality and concentration using Tapestation.

Single-cell RNA-seq data analysis

Raw sequencing data generated from the Illumina NovaSeq platform were processed using the Cell Ranger pipeline (version 8.0.1, 10X Genomics). This pipeline performed demultiplexing, alignment to the reference genome (hg GRCh38 or mm39), and barcode processing to produce gene–cell matrices for downstream analysis. To ensure consistent filtering, datasets from in vivo samples treated with either vehicle or drug were merged into a single dataset.

Unsupervised clustering of single-cell RNA sequencing (scRNA-seq) data was performed using the R package Seurat[121] (version 5.3.0). Cells were filtered based on quality metrics, excluding those with low or high unique molecular identifier (UMI) counts, low or high gene numbers, or elevated mitochondrial gene expression (>10%). Gene expression levels were normalized to 10,000 UMIs per cell and log-transformed by adding 1 to the expression matrix. Highly variable genes (top 2000) were identified using Seurat's "vst" method, which were subsequently used for principal component analysis (PCA). The first 30 principal components (PCs) were utilized for dimensionality reduction via uniform manifold approximation and projection (UMAP) and clustering. Cell type markers were applied to annotate tumor cell types within each cluster.

Drug signature score calculation in normal immune cells

Context-matched gene signatures induced by regorafenib and mirdametinib were curated from bone marrow dataset (regorafenib: SCP_87407; mirdametinib: SCP_86814; Table S15) using cutoffs of $|logFC| > 1.5$ and p-value < 0.05. This yielded 48 upregulated and 55 downregulated genes for mirdametinib, and 58 upregulated and 93 downregulated genes for regorafenib.

For normal cells, gene expression values in each single cell were standardized, and the drug signature score was calculated by subtracting the ssGSEA score of the upregulated gene set from the ssGSEA score of the downregulated gene set for the mirdametinib-regorafenib combination.

Cell–cell interaction analysis

Cell–cell interaction analysis was conducted using samples from 16 mice (4 mice per treatment arm) profiled with the 10x Flex Gene Expression platform. Interactions were analyzed using CellChat (V2.1.2), focusing on secreted signaling ligand-receptor pairs from the CellChatDB database. The selected cell types included: "Tcm," "Teffector," "Tex," "Tfh," "Th17," "Treg," "Mono," "Macrophage" "Microglia" and "Tumor" The number and strength of inferred interactions were analyzed between the 10 selected cell types. Differential interaction strength was compared between each treatment arm and the control group. Additionally, the relative interaction strength and information flow for specific receptor-ligand signaling pathways were assessed.

DATA AVAILABILITY

The 10x Genomics single-cell RNA-seq data generated in this study are available from NCBI GEO under accession numbers GSE308633 (access token: mzolmweuvpazdgj), GSE308635 (access token: arqluekyxtylbql), GSE308649 (access token: clibaaqyvrevzcn), and GSE308692 (access token: kzurmeyidfybtsh). Additional resources include the SINBA medulloblastoma portal (https://yulab-stjude.shinyapps.io/SINBA_MB), the normal glutamatergic lineage developmental reference portal (https://scminer.stjude.org/study/Glutamatergic-lineage), and the medulloblastoma patient scRNA-seq portal (https://scminer.stjude.org/study/GSE155446). 10x Genomics scRNA-seq data from developing human cerebellum and medulloblastoma patients were obtained from Luo et al.[66] and are also available via the China National GeneBank Data Base (CNP0002781). Additional medulloblastoma patient 10x scRNA-seq data were downloaded from GEO (GSE155446), and Smart-seq2 scRNA-seq data from GEO (GSE119926).

CODE AVAILABILITY

SINBA package is available on GitHub (https://github.com/jyyulab/SINBA).

REFERENCES

1. Siegel DA*, et al.* Pediatric cancer mortality and survival in the United States, 2001-2016. *Cancer* **126**, 4379–4389 (2020).

2. Kool M*, et al.* Molecular subgroups of medulloblastoma: an international meta-analysis of transcriptome, genetic aberrations, and clinical data of WNT, SHH, Group 3, and Group 4 medulloblastomas. *Acta Neuropathol* **123**, 473–484 (2012).

3. Taylor MD*, et al.* Molecular subgroups of medulloblastoma: the current consensus. *Acta Neuropathol* **123**, 465–472 (2012).

4. Gajjar A*, et al.* Risk-adapted craniospinal radiotherapy followed by high-dose chemotherapy and stem-cell rescue in children with newly diagnosed medulloblastoma (St Jude Medulloblastoma-96): long-term results from a prospective, multicentre trial. *The Lancet Oncology* **7**, 813–820 (2006).

5. Gajjar A*, et al.* Outcomes by Clinical and Molecular Features in Children With Medulloblastoma Treated With Risk-Adapted Therapy: Results of an International Phase III Trial (SJMB03). *J Clin Oncol*, JCO2001372 (2021).

6. Koschmann C, Bloom K, Upadhyaya S, Geyer JR, Leary SE. Survival After Relapse of Medulloblastoma. *J Pediatr Hematol Oncol* **38**, 269–273 (2016).

7. Sabel M*, et al.* Relapse patterns and outcome after relapse in standard risk medulloblastoma: a report from the HIT-SIOP-PNET4 study. *J Neurooncol* **129**, 515–524 (2016).

8. Aldape K*, et al.* Challenges to curing primary brain tumours. *Nat Rev Clin Oncol* **16**, 509–520 (2019).

9. Northcott PA*, et al.* The whole-genome landscape of medulloblastoma subtypes. *Nature* **547**, 311–317 (2017).

10. Ibrahim YH*, et al.* PI3K inhibition impairs BRCA1/2 expression and sensitizes BRCA-proficient triple-negative breast cancer to PARP inhibition. *Cancer Discov* **2**, 1036–1047 (2012).

11. Robert C*, et al.* Improved overall survival in melanoma with combined dabrafenib and trametinib. *N Engl J Med* **372**, 30–39 (2015).

12. DiNardo CD*, et al.* Azacitidine and Venetoclax in Previously Untreated Acute Myeloid Leukemia. *N Engl J Med* **383**, 617–629 (2020).

13. Turner NC*, et al.* Palbociclib in Hormone-Receptor-Positive Advanced Breast Cancer. *N Engl J Med* **373**, 209–219 (2015).

14. Mok TSK*, et al.* Pembrolizumab versus chemotherapy for previously untreated, PD-L1-expressing, locally advanced or metastatic non-small-cell lung cancer (KEYNOTE-042): a randomised, open-label, controlled, phase 3 trial. *Lancet* **393**, 1819–1830 (2019).

15. Larkin J, Hodi FS, Wolchok JD. Combined Nivolumab and Ipilimumab or Monotherapy in Untreated Melanoma. *N Engl J Med* **373**, 1270–1271 (2015).

16. Chen EX*, et al.* Effect of Combined Immune Checkpoint Inhibition vs Best Supportive Care Alone in Patients With Advanced Colorectal Cancer: The Canadian Cancer Trials Group CO.26 Study. *JAMA Oncol* **6**, 831–838 (2020).

17. Eng C*, et al.* Atezolizumab with or without cobimetinib versus regorafenib in previously treated metastatic colorectal cancer (IMblaze370): a multicentre, open-label, phase 3, randomised, controlled trial. *Lancet Oncol* **20**, 849–861 (2019).

18. Pei Y*, et al.* HDAC and PI3K Antagonists Cooperate to Inhibit Growth of MYC-Driven Medulloblastoma. *Cancer Cell* **29**, 311–323 (2016).

19. Preuer K, Lewis RPI, Hochreiter S, Bender A, Bulusu KC, Klambauer G. DeepSynergy: predicting anti-cancer drug synergy with Deep Learning. *Bioinformatics* **34**, 1538–1546 (2018).

20. Liu W, Wang Z, Liu X, Zeng N, Liu Y, Alsaadi FE. A survey of deep neural network architectures and their applications. *Neurocomputing* **234**, 11–26 (2017).

21. Adam G, Rampasek L, Safikhani Z, Smirnov P, Haibe-Kains B, Goldenberg A. Machine learning approaches to drug response prediction: challenges and recent progress. *NPJ Precis Oncol* **4**, 19 (2020).

22. Jassim A*, et al.* Gene context drift identifies drug targets to mitigate cancer treatment resistance. *Cancer Cell* **43**, 1608–1621 e1609 (2025).

23. Bansal M*, et al.* A community computational challenge to predict the activity of pairs of compounds. *Nat Biotechnol* **32**, 1213–1222 (2014).

24. Kuenzi BM*, et al.* Predicting Drug Response and Synergy Using a Deep Learning Model of Human Cancer Cells. *Cancer Cell* **38**, 672–684 e676 (2020).

25. Robinson G*, et al.* Novel mutations target distinct subgroups of medulloblastoma. *Nature* **488**, 43–48 (2012).

26. Califano A, Alvarez MJ. The recurrent architecture of tumour initiation, progression and drug sensitivity. *Nat Rev Cancer* **17**, 116–130 (2017).

27. Piovan E*, et al.* Direct reversal of glucocorticoid resistance by AKT inhibition in acute lymphoblastic leukemia. *Cancer Cell* **24**, 766–776 (2013).

28. Autry RJ*, et al.* Integrative genomic analyses reveal mechanisms of glucocorticoid resistance in acute lymphoblastic leukemia. *Nature Cancer* **1**, 329–344 (2020).

29. Zeleke TZ*, et al.* Network-based assessment of HDAC6 activity predicts preclinical and clinical responses to the HDAC6 inhibitor ricolinostat in breast cancer. *Nat Cancer* **4**, 257–275 (2023).

30. Gocho Y*, et al.* Network-based systems pharmacology reveals heterogeneity in LCK and BCL2 signaling and therapeutic sensitivity of T-cell acute lymphoblastic leukemia. *Nature Cancer*, (2021).

31. Ianevski A, Giri AK, Aittokallio T. SynergyFinder 2.0: visual analytics of multi-drug combination synergies. *Nucleic Acids Res* **48**, W488–W493 (2020).

32. Yadav B, Wennerberg K, Aittokallio T, Tang J. Searching for Drug Synergy in Complex Dose-Response Landscapes Using an Interaction Potency Model. *Comput Struct Biotechnol J* **13**, 504–513 (2015).

33. Meng F, Xi Y, Huang J, Ayers PW. A curated diverse molecular database of blood-brain barrier permeability with chemical descriptors. *Sci Data* **8**, 289 (2021).

34. Wishart DS*, et al.* DrugBank 5.0: a major update to the DrugBank database for 2018. *Nucleic Acids Res* **46**, D1074–D1082 (2018).

35. Cheng F, Kovacs IA, Barabasi AL. Network-based prediction of drug combinations. *Nat Commun* **10**, 1197 (2019).

36. Subramanian A*, et al.* A Next Generation Connectivity Map: L1000 Platform and the First 1,000,000 Profiles. *Cell* **171**, 1437–1452 e1417 (2017).

37. Corsello SM*, et al.* The Drug Repurposing Hub: a next-generation drug library and information resource. *Nat Med* **23**, 405–408 (2017).

38. Cotto KC*, et al.* DGIdb 3.0: a redesign and expansion of the drug-gene interaction database. *Nucleic Acids Res* **46**, D1068–D1073 (2018).

39. Cannon M*, et al.* DGIdb 5.0: rebuilding the drug-gene interaction database for precision medicine and drug discovery platforms. *Nucleic Acids Res* **52**, D1227–D1235 (2024).

40. Griffith M*, et al.* DGIdb: mining the druggable genome. *Nat Methods* **10**, 1209–1210 (2013).

41. Khatamian A, Paull EO, Califano A, Yu J. SJARACNe: a scalable software tool for gene network reverse engineering from big data. *Bioinformatics* **35**, 2165–2166 (2019).

42. Northcott PA*, et al.* Subgroup-specific structural variation across 1,000 medulloblastoma genomes. *Nature* **488**, 49–56 (2012).

43. de Bont JM*, et al.* Differential expression and prognostic significance of SOX genes in pediatric medulloblastoma and ependymoma identified by microarray analysis. *Neuro Oncol* **10**, 648–660 (2008).

44. Ashburner M*, et al.* Gene Ontology: tool for the unification of biology. *Nature Genetics* **25**, 25–29 (2000).

45. Dong X*, et al.* NetBID2 provides comprehensive hidden driver analysis. *Nat Commun* **14**, 2581 (2023).

46. Cavalli FMG*, et al.* Intertumoral Heterogeneity within Medulloblastoma Subgroups. *Cancer Cell* **31**, 737–754 e736 (2017).

47. Archer TC*, et al.* Proteomics, Post-translational Modifications, and Integrative Analyses Reveal Molecular Heterogeneity within Medulloblastoma Subgroups. *Cancer Cell* **34**, 396–410 e398 (2018).

48. Kort A, Durmus S, Sparidans RW, Wagenaar E, Beijnen JH, Schinkel AH. Brain and Testis Accumulation of Regorafenib is Restricted by Breast Cancer Resistance Protein (BCRP/ABCG2) and P-glycoprotein (P-GP/ABCB1). *Pharm Res* **32**, 2205–2216 (2015).

49. Jiang J*, et al.* Regorafenib induces lethal autophagy arrest by stabilizing PSAT1 in glioblastoma. *Autophagy* **16**, 106–122 (2020).

50. Zeiner PS*, et al.* Regorafenib CSF Penetration, Efficacy, and MRI Patterns in Recurrent Malignant Glioma Patients. *J Clin Med* **8**, (2019).

51. Freeman BB, 3rd, Yang L, Rankovic Z. Practical approaches to evaluating and optimizing brain exposure in early drug discovery. *Eur J Med Chem* **182**, 111643 (2019).

52. de Gooijer MC, Zhang P, Weijer R, Buil LCM, Beijnen JH, van Tellingen O. The impact of P-glycoprotein and breast cancer resistance protein on the brain pharmacokinetics and pharmacodynamics of a panel of MEK inhibitors. *Int J Cancer* **142**, 381–391 (2018).

53. He C*, et al.* Patient-derived models recapitulate heterogeneity of molecular signatures and drug response in pediatric high-grade glioma. *Nat Commun* **12**, 4089 (2021).

54. Klaeger S*, et al.* The target landscape of clinical kinase drugs. *Science* **358**, (2017).

55. Kanehisa M, Goto S. KEGG: kyoto encyclopedia of genes and genomes. *Nucleic Acids Res* **28**, 27–30 (2000).

56. Ghandi M*, et al.* Next-generation characterization of the Cancer Cell Line Encyclopedia. *Nature* **569**, 503–508 (2019).

57. Pilarczyk M*, et al.* Connecting omics signatures and revealing biological mechanisms with iLINCS. *Nat Commun* **13**, 4678 (2022).

58. Smith KS*, et al.* Patient-derived orthotopic xenografts of pediatric brain tumors: a St. Jude resource. *Acta Neuropathol* **140**, 209–225 (2020).

59. McLeod C*, et al.* St. Jude Cloud: A Pediatric Cancer Genomic Data-Sharing Ecosystem. *Cancer Discov* **11**, 1082–1099 (2021).

60. Padovani L, Horan G, Ajithkumar T. Radiotherapy Advances in Paediatric Medulloblastoma Treatment. *Clin Oncol (R Coll Radiol)* **31**, 171–181 (2019).

61. Hill RM*, et al.* Time, pattern, and outcome of medulloblastoma relapse and their association with tumour biology at diagnosis and therapy: a multicentre cohort study. *The Lancet Child & Adolescent Health* **4**, 865–874 (2020).

62. Hovestadt V*, et al.* Resolving medulloblastoma cellular architecture by single-cell genomics. *Nature*, (2019).

63. Riemondy KA*, et al.* Neoplastic and immune single-cell transcriptomics define subgroup-specific intra-tumoral heterogeneity of childhood medulloblastoma. *Neuro Oncol* **24**, 273–286 (2022).

64. Hendrikse LD*, et al.* Failure of human rhombic lip differentiation underlies medulloblastoma formation. *Nature* **609**, 1021–1028 (2022).

65. Smith KS*, et al.* Unified rhombic lip origins of group 3 and group 4 medulloblastoma. *Nature* **609**, 1012–1020 (2022).

66. Luo Z*, et al.* Human fetal cerebellar cell atlas informs medulloblastoma origin and oncogenesis. *bioRxiv*, 2022.2008.2017.504304 (2022).

67. Gibson P*, et al.* Subtypes of medulloblastoma have distinct developmental origins. *Nature* **468**, 1095–1099 (2010).

68. Erickson AW*, et al.* Mapping the developmental profile of ventricular zone-derived neurons in the human cerebellum. *Proc Natl Acad Sci U S A* **122**, e2415425122 (2025).

69. Sepp M*, et al.* Cellular development and evolution of the mammalian cerebellum. *Nature*, (2024).

70. Aldinger KA*, et al.* Spatial and cell type transcriptional landscape of human cerebellar development. *Nat Neurosci* **24**, 1163–1175 (2021).

71. Lu S*, et al.* Transcriptome size matters for single-cell RNA-seq normalization and bulk deconvolution. *Nat Commun* **16**, 1246 (2025).

72. Luo Z*, et al.* Genomic and Transcriptomic Analyses Reveals ZNF124 as a Critical Regulator in Highly Aggressive Medulloblastomas. *Front Cell Dev Biol* **9**, 634056 (2021).

73. Pan Q*, et al.* scMINER: a mutual information-based framework for clustering and hidden driver inference from single-cell transcriptomics data. *Nat Commun* **16**, 4305 (2025).

74. Luo Z*, et al.* Loss of phosphatase CTDNEP1 potentiates aggressive medulloblastoma by triggering MYC amplification and genomic instability. *Nat Commun* **14**, 762 (2023).

75. Bae J*, et al.* Targeting LAG3/GAL-3 to overcome immunosuppression and enhance anti-tumor immune responses in multiple myeloma. *Leukemia* **36**, 138–154 (2022).

76. Blum JS, Wearsch PA, Cresswell P. Pathways of antigen processing. *Annu Rev Immunol* **31**, 443–473 (2013).

77. Chen YH*, et al.* Regorafenib enhances M1/M2 macrophage polarization by inhibiting the secretion of plasminogen activator inhibitor-1 in head and neck squamous cell carcinoma. *Life Sci* **358**, 123147 (2024).

78. Allen F*, et al.* CCL3 augments tumor rejection and enhances CD8(+) T cell infiltration through NK and CD103(+) dendritic cell recruitment via IFNgamma. *Oncoimmunology* **7**, e1393598 (2018).

79. Kang TG, Park HJ, Moon J, Lee JH, Ha SJ. Enriching CCL3 in the Tumor Microenvironment Facilitates T cell Responses and Improves the Efficacy of Anti-PD-1 Therapy. *Immune Netw* **21**, e23 (2021).

80. Eberlein J*, et al.* Chemokine Signatures of Pathogen-Specific T Cells I: Effector T Cells. *J Immunol* **205**, 2169–2187 (2020).

81. Wang BL*, et al.* CXCR6 is required for antitumor efficacy of intratumoral CD8 T cell. *Journal for Immunotherapy of Cancer* **9**, (2021).

82. Di Pilato M*, et al.* CXCR6 positions cytotoxic T cells to receive critical survival signals in the tumor microenvironment. *Cell* **184**, 4512–+ (2021).

83. Muthuswamy R*, et al.* CXCR6 by increasing retention of memory CD8 T cells in the ovarian tumor microenvironment promotes immunosurveillance and control of ovarian cancer. *Journal for Immunotherapy of Cancer* **9**, (2021).

84. Seo YD*, et al.* Mobilization of CD8⁺ T Cells via CXCR4 Blockade Facilitates PD-1 Checkpoint Therapy in Human Pancreatic Cancer. *Clinical Cancer Research* **25**, 3934–3945 (2019).

85. Liu SY, Zhang W, Liu K, Wang YC. CD160 expression on CD8 T cells is associated with active effector responses but limited activation potential in pancreatic cancer. *Cancer Immunol Immun* **69**, 789–797 (2020).

86. Duhen T*, et al.* Co-expression of CD39 and CD103 identifies tumor-reactive CD8 T cells in human solid tumors. *Nature Communications* **9**, (2018).

87. Lamichhane R*, et al.* TCR- or Cytokine-Activated CD8(+) Mucosal-Associated Invariant T Cells Are Rapid Polyfunctional Effectors That Can Coordinate Immune Responses. *Cell Rep* **28**, 3061–3076 e3065 (2019).

88. Jin SQ*, et al.* Inference and analysis of cell-cell communication using CellChat. *Nature Communications* **12**, (2021).

89. Huang L*, et al.* Systems biology-based drug repositioning identifies digoxin as a potential therapy for groups 3 and 4 medulloblastoma. *Sci Transl Med* **10**, (2018).

90. Hovestadt V, Ayrault O, Swartling FJ, Robinson GW, Pfister SM, Northcott PA. Medulloblastomics revisited: biological and clinical insights from thousands of patients. *Nat Rev Cancer* **20**, 42–56 (2020).

91. Visvanathan A*, et al.* Early rhombic lip Protogenin(+ve) stem cells in a human-specific neurovascular niche initiate and maintain group 3 medulloblastoma. *Cell* **187**, 4733–4750 e4726 (2024).

92. Jessa S*, et al.* Stalled developmental programs at the root of pediatric brain tumors. *Nat Genet* **51**, 1702–1713 (2019).

93. Xie X*, et al.* Converging mechanism of UM171 and KBTBD4 neomorphic cancer mutations. *Nature* **639**, 241–249 (2025).

94. Lombardi G*, et al.* Regorafenib compared with lomustine in patients with relapsed glioblastoma (REGOMA): a multicentre, open-label, randomised, controlled, phase 2 trial. *The Lancet Oncology* **20**, 110–119 (2019).

95. Weiss BD*, et al.* NF106: A Neurofibromatosis Clinical Trials Consortium Phase II Trial of the MEK Inhibitor Mirdametinib (PD-0325901) in Adolescents and Adults With NF1-Related Plexiform Neurofibromas. *J Clin Oncol*, JCO2002220 (2021).

96. Banerjee A*, et al.* A phase I study of AZD6244 in children with recurrent or refractory low-grade gliomas: A Pediatric Brain Tumor Consortium report. *Journal of Clinical Oncology* **32**, (2014).

97. Andrew N*, et al.* Phase 1 Study of Fluvastatin-Celecoxib Combination in Children with Relapsing/Refractory Optico-Chiasmatic Low-Grade Glioma or High-Grade Gliomas (Fluvabrex): Final Results. *Neuro-Oncology* **22**, 305–306 (2020).

98. Corcoran RB*, et al.* Combined BRAF and MEK Inhibition With Dabrafenib and Trametinib in BRAF V600-Mutant Colorectal Cancer. *J Clin Oncol* **33**, 4023–4031 (2015).

99. Wu CS*, et al.* Curcumin functions as a MEK inhibitor to induce a synthetic lethal effect on KRAS mutant colorectal cancer cells receiving targeted drug regorafenib. *J Nutr Biochem* **74**, 108227 (2019).

100. Lau DK*, et al.* Rapid Resistance of FGFR-driven Gastric Cancers to Regorafenib and Targeted FGFR Inhibitors can be Overcome by Parallel Inhibition of MEK. *Mol Cancer Ther* **20**, 704–715 (2021).

101. Adamopoulos C*, et al.* Exploiting Allosteric Properties of RAF and MEK Inhibitors to Target Therapy-Resistant Tumors Driven by Oncogenic BRAF Signaling. *Cancer Discov*, (2021).

102. MacDonald TJ*, et al.* Expression profiling of medulloblastoma: PDGFRA and the RAS/MAPK pathway as therapeutic targets for metastatic disease. *Nature Genetics* **35**, 287–287 (2003).

103. Abeysundara N*, et al.* Metastatic medulloblastoma remodels the local leptomeningeal microenvironment to promote further metastatic colonization and growth. *Nat Cell Biol*, (2025).

104. da Cunha Jaeger M*, et al.* HDAC and MAPK/ERK Inhibitors Cooperate To Reduce Viability and Stemness in Medulloblastoma. *J Mol Neurosci* **70**, 981–992 (2020).

105. Bakhshinyan D*, et al.* Temporal profiling of therapy resistance in human medulloblastoma identifies novel targetable drivers of recurrence. *Sci Adv* **7**, eabi5568 (2021).

106. Li S*, et al.* Liposomal Honokiol induces ROS-mediated apoptosis via regulation of ERK/p38-MAPK signaling and autophagic inhibition in human medulloblastoma. In: *Signal Transduct Target Ther*). 20220221 edn (2022).

107. Ebert PJR*, et al.* MAP Kinase Inhibition Promotes T Cell and Anti-tumor Activity in Combination with PD-L1 Checkpoint Blockade. *Immunity* **44**, 609–621 (2016).

108. Liu J*, et al.* Immunomodulatory effects of regorafenib: Enhancing the efficacy of anti-PD-1/PD-L1 therapy. *Front Immunol* **13**, 992611 (2022).

109. Ou DL*, et al.* Regorafenib enhances antitumor immunity via inhibition of p38 kinase/Creb1/Klf4 axis in tumor-associated macrophages. *J Immunother Cancer* **9**, (2021).

110. Margolin AA*, et al.* ARACNE: an algorithm for the reconstruction of gene regulatory networks in a mammalian cellular context. *BMC Bioinformatics* **7 Suppl 1**, S7 (2006).

111. Scrucca L. GA: A Package for Genetic Algorithms in R. *Journal of Statistical Software* **53**, 1–37 (2013).

112. Jonchere B*, et al.* Combination of Ribociclib with BET-Bromodomain and PI3K/mTOR Inhibitors for Medulloblastoma Treatment In Vitro and In Vivo. *Mol Cancer Ther* **22**, 37–51 (2023).

113. Ritz C, Baty F, Streibig JC, Gerhard D. Dose-Response Analysis Using R. *PLoS One* **10**, e0146021 (2015).

114. Zheng S*, et al.* SynergyFinder Plus: Toward Better Interpretation and Annotation of Drug Combination Screening Datasets. *Genomics Proteomics Bioinformatics* **20**, 587–596 (2022).

115. Milde T*, et al.* HD-MB03 is a novel Group 3 medulloblastoma model demonstrating sensitivity to histone deacetylase inhibitor treatment. *J Neurooncol* **110**, 335–348 (2012).

116. Bandopadhayay P*, et al.* BET bromodomain inhibition of MYC-amplified medulloblastoma. *Clin Cancer Res* **20**, 912–925 (2014).

117. Kawauchi D*, et al.* A mouse model of the most aggressive subgroup of human medulloblastoma. *Cancer Cell* **21**, 168–180 (2012).

118. Xie J*, et al.* ATM inhibition enhances the efficacy of radiation across distinct molecular subgroups of pediatric high-grade glioma. *Neuro Oncol* **25**, 1828–1841 (2023).

119. Street K*, et al.* Slingshot: cell lineage and pseudotime inference for single-cell transcriptomics. *BMC Genomics* **19**, 477 (2018).

120. Qiu X*, et al.* Reversed graph embedding resolves complex single-cell trajectories. *Nat Methods* **14**, 979–982 (2017).

121. Hao Y*, et al.* Dictionary learning for integrative, multimodal and scalable single-cell analysis. *Nat Biotechnol* **42**, 293–304 (2024).

1475
1476

ACKNOWLEDGEMENTS

We extend our sincere gratitude to Sarah August for her exceptional contributions to this project, including her dedicated efforts in manuscript preparation and revision, her creative input, and her expertise in data presentation. We are also deeply grateful to the following St. Jude Children's Research Hospital core facilities for their consistent support and expertise: the Center for *In Vivo* Imaging and Therapy (Melissa Johnson and team), the Animal Research Center (Chandra Savage and team), the Flow Cytometry and Cell Sorting Core, and the Comparative Pathology Core. We thank Dr. Anang A. Shelat for his expert assistance in analyzing the high-throughput screening data and Dr. Suzanne J. Baker for her insightful suggestions on the design of our *in vivo* experiments. We are also grateful to Dr. Till Milde for sharing the HDMB03 line and Dr. Q. Richard Lu for generously sharing multiple MB models including CTD. This work is supported, in part, by National Institutes of Health grants R01GM134382 (to J.Y.), U01CA264610 (to J.Y.), and U01CA281868 (to J.Y.), by the COOKIES FOR KIDS CANCER translational award (to J.Y.), by the Big Hope Little Warrior Cancer Foundation, and by the American Lebanese Syrian Associated Charities.

AUTHOR CONTRIBUTIONS

J.Y. and J.L. conceptualized the study; J.L., X.Y. and M.Z. performed all the experiments with B.B., B.M.J., W.L., and X.F.; J.L. performed all the data analysis with X.Y., M.Z., X.D., H.Z., B.M.J., L.Y., B.B.F.III, A.W. and R.J.; T.C., G.W.R., M.F.R., T.E.M. and A.G. provided relevant intellectual input and edited the manuscript. J.L., X.Y., and M.Z. interpreted the results. J.L., X.Y., M.Z. and J.Y. wrote the manuscript. All the authors reviewed and commented on the manuscript.

COMPETING INTERESTS

The authors declare no competing interests.

FIGURES

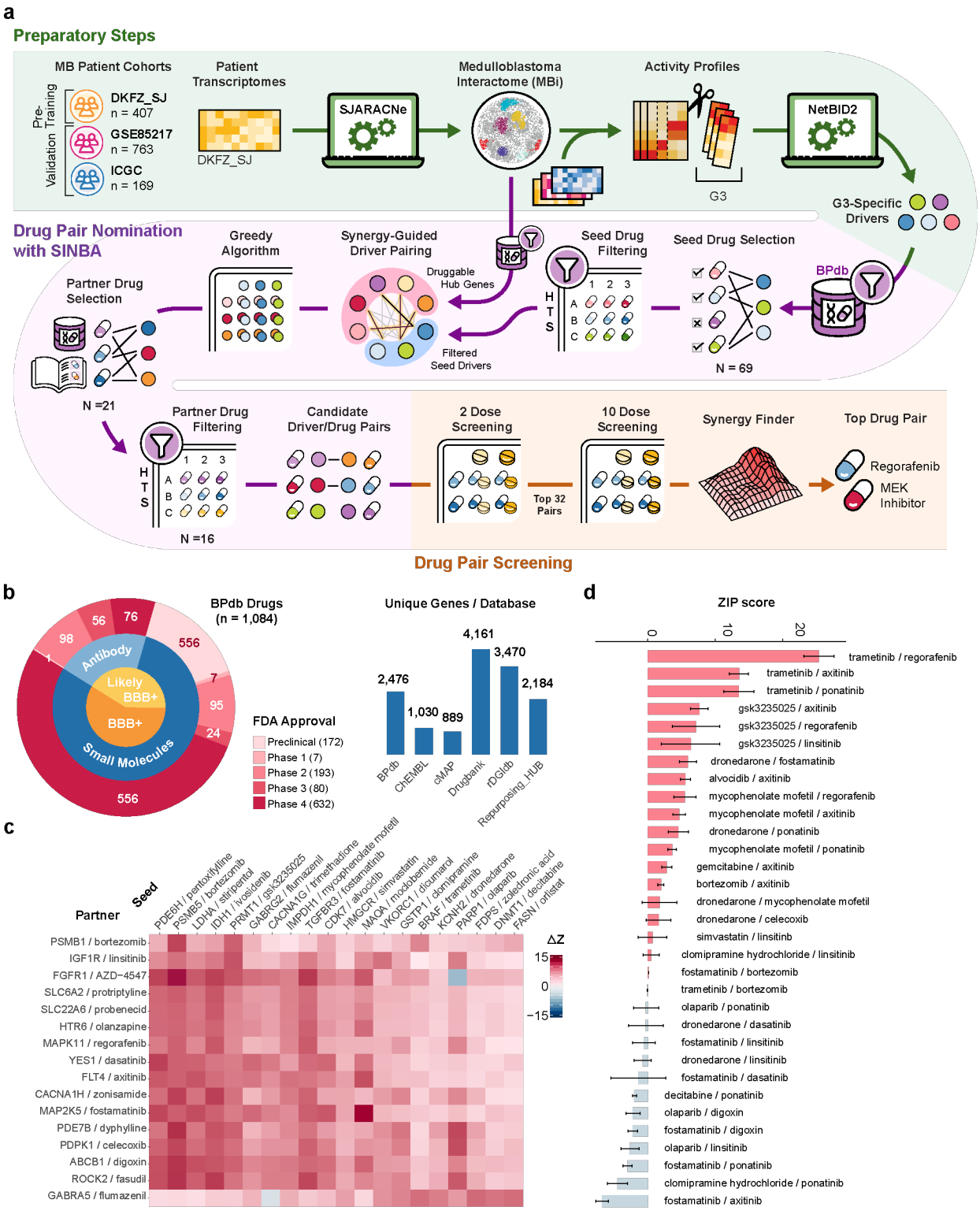


Figure 1. SINBA leverages gene activity data and knowledge-based drug databases to predict and guide screening of synergistic drug pairs for high-risk medulloblastoma.

a Overview of the SINBA workflow for identifying synergistic drug combinations in medulloblastoma. Preparatory steps include using SJARACNe to generate a disease-specific gene interaction network and NetBID2 to identify subtype-specific driver genes. SINBA then selects drugs for single-agent screening before predicting synergistic drug pairs for combination testing. Finally, combination screening and synergy analysis identify promising drug pairs for validation. **b** Breakdown of the Brain Penetrant Database (BPdb), a manually curated repository of potential and clinically validated blood-brain barrier penetrating (BBB+) drugs. SINBA integrates the BPdb with five additional drug-gene interaction databases for comprehensive target annotation. **c** An optimized driver pair matrix based on SINBA's predictions of synergy in silico. Seed drivers (columns) and partner drivers (rows) are listed with their respective drugs. Delta Z-scores indicate the predicted synergy of each driver pair. **d** Synergy analysis of the results of 10-dose combination screening. Synergy is expressed as a Zero Interaction Potency (ZIP) score. Data are represented as the mean ± SEM.

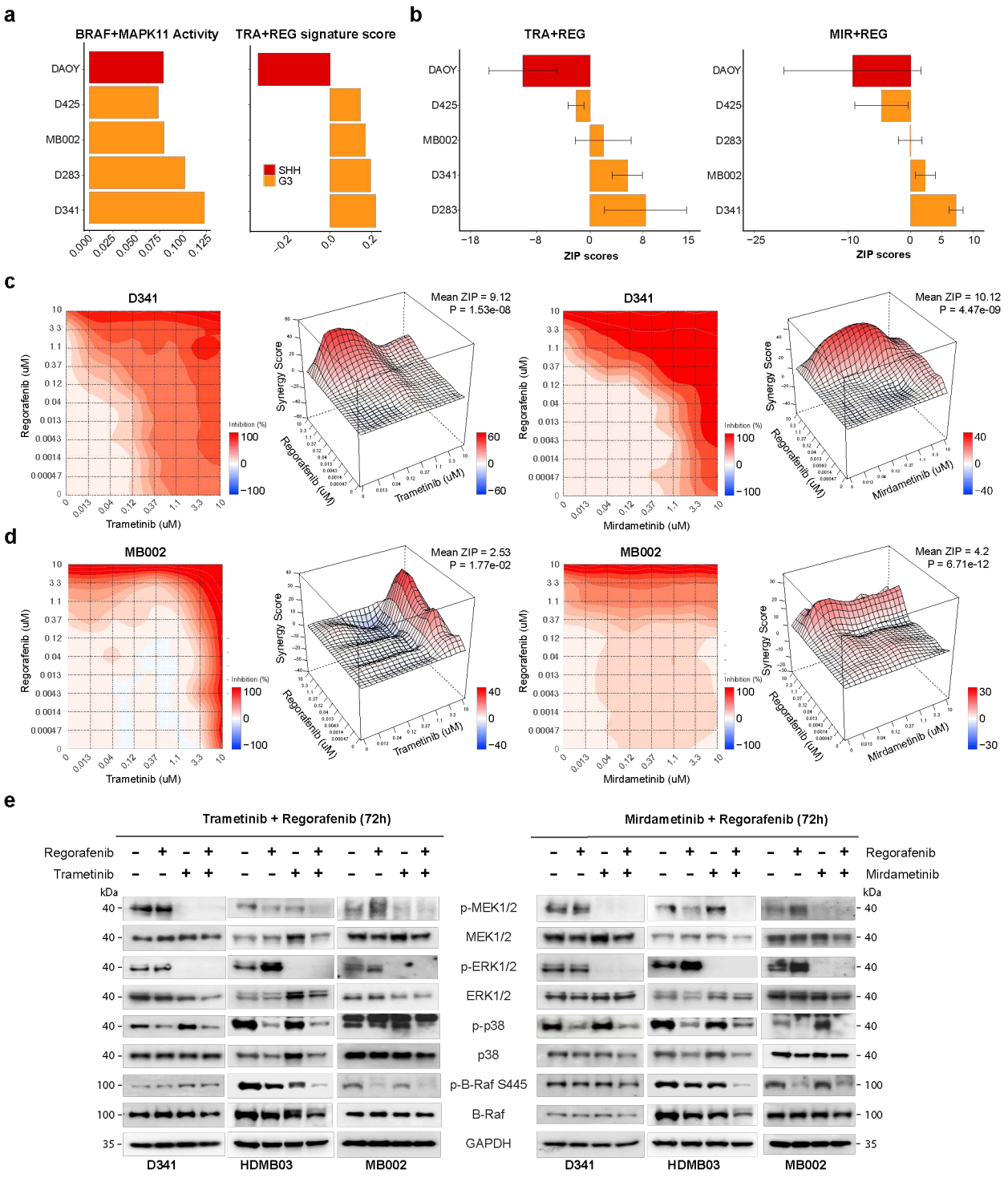


Figure 2. Synergistic and on-target effects of MEK inhibitor and regorafenib combination in human G3 MB models. **a** Left panel shows the combined activities of BRAF and MAPK11 in five human MB cell lines. Right panel shows those cell lines' drug sensitivity scores for trametinib

(TRA) plus regorafenib (REG). **b** Ranked ZIP scores for two regorafenib + MEK inhibitor (trametinib or mirdametinib) combinations in human MB cell lines. Data are represented as mean ± SEM. **c** Cell growth inhibition contour plots and synergy landscapes for drug-dose combinations of regorafenib and trametinib (left) and regorafenib and mirdametinib (right) in D341 cells. **d** Cell growth inhibition contour plots and synergy landscapes for drug-dose combinations of regorafenib and trametinib (left) and regorafenib and mirdametinib (right) in MB002 cells. **e** Western blot analysis comparing total and phosphorylated MEK, ERK, p38, and BRAF following single agent and combination treatment with regorafenib + trametinib (left) or regorafenib + mirdametinib (right) at indicated time points.

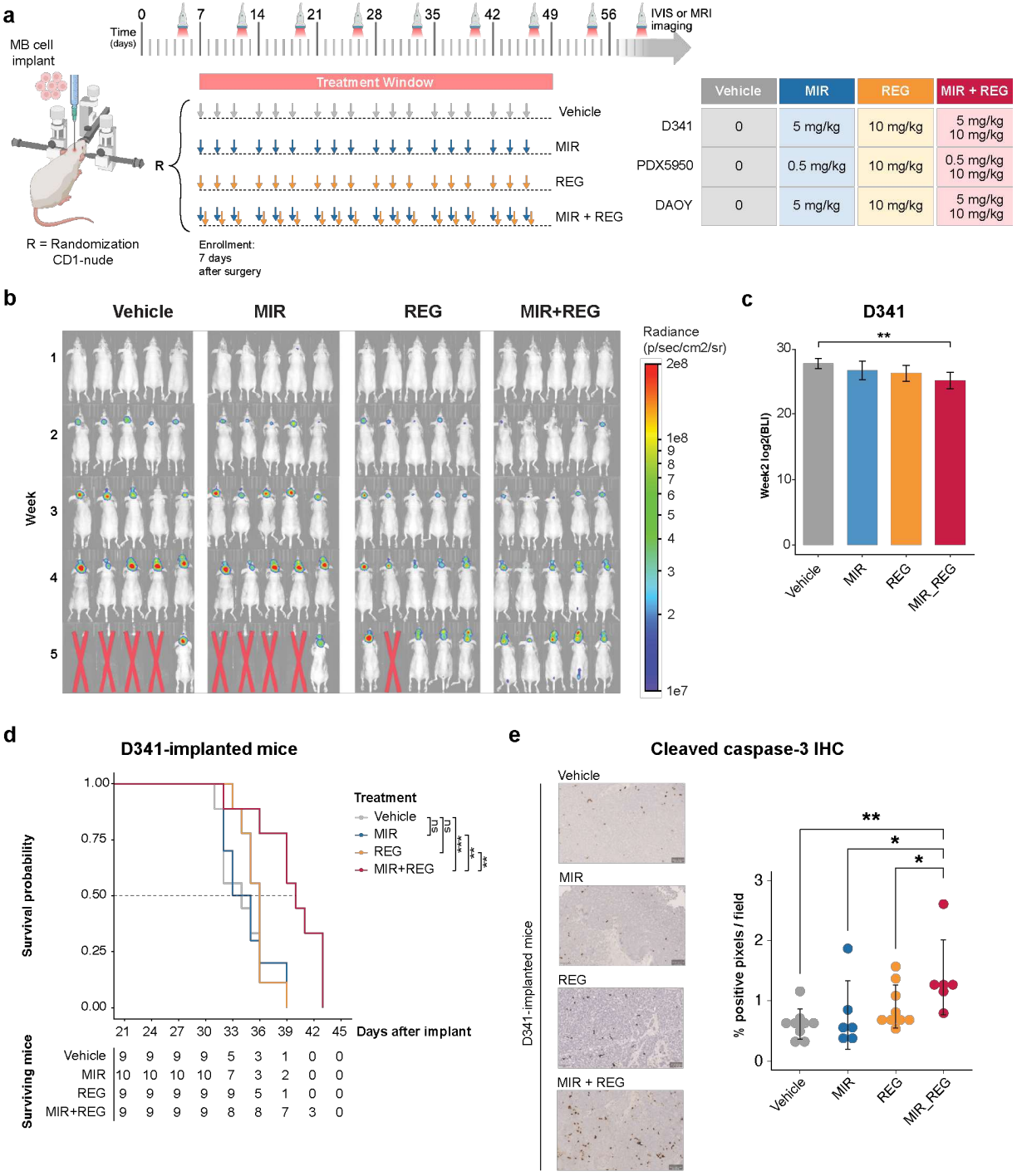


Figure 3. MEK inhibitor and regorafenib combination has synergistic anti-tumor efficacy *in vivo* with G3 cell line model. **a** Schematic of experimental design for drug administration and imaging in CD-1 nude mice implanted intracranially with D341, PDX5950, or DAOY tumor cells (created with BioRender.com). Mice were randomized to receive vehicle (p.o.), mirdametinib (5

mg/kg or 0.5 mg/kg, p.o.), regorafenib (10 mg/kg, p.o.), or the combination, starting one week post-implantation and continuing three times per week for six weeks. IVIS or MRI imaging was performed weekly starting one week after surgery. **b** Representative *in vivo* bioluminescent images of mice bearing orthotopic D341 tumors from weeks 1 to 5 post-implantation. **c** Quantification of bioluminescence signal (BLI) at week 2 post-treatment in the D341 model, showing significant tumor growth reduction in the combination group. Data are presented as mean ± SEM. **d** Kaplan–Meier survival curves for mice implanted with D341 cells and treated as described in (**b**). Group sizes (n) are indicated in the risk table; log-rank test results: *P < 0.05, **P < 0.01, ***P < 0.001; ns, not significant. **e** Left: Representative IHC staining for cleaved caspase-3 in D341 tumors. Right: Quantification of cleaved caspase-3-positive cells. Data are presented as mean ± SEM. *P < 0.05; **P < 0.01.

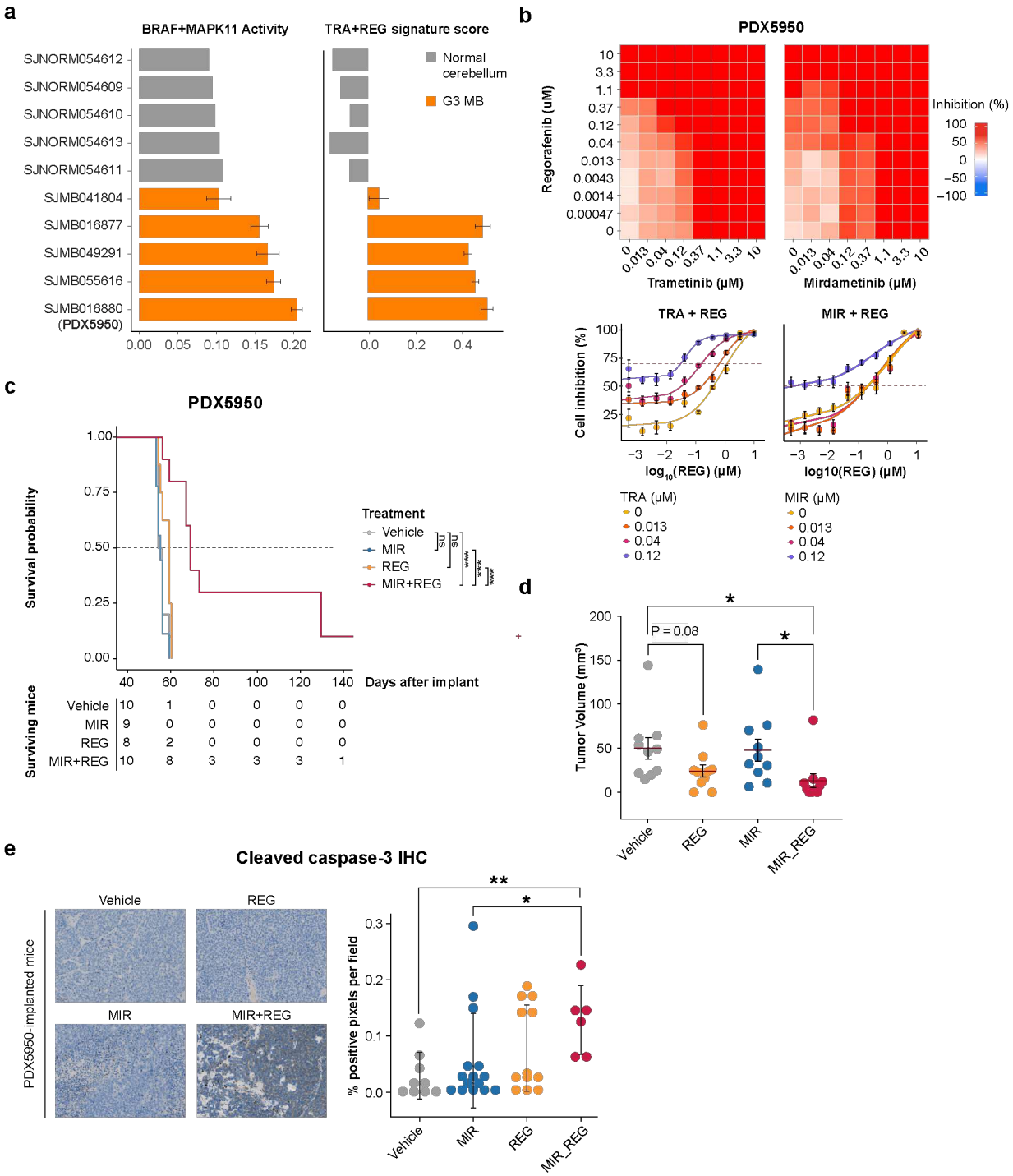


Figure 4. MEK inhibitor and regorafenib combination has synergistic anti-tumor efficacy *in vivo* with patient derived orthotopic xenograft model. **a** Left panel shows the combined activities of BRAF and MAPK11 in normal cerebellum and human G3 MB PDOX models. Right panel shows their drug sensitivity scores for trametinib (TRA) plus regorafenib (REG). **b** Top:

Heatmap of PDX5950 cell viability with regorafenib and MEK inhibitor combinations. Bottom: Dose–response curves for regorafenib in combination with fixed concentrations of trametinib or mirdametinib. **c** Kaplan–Meier survival curves for mice implanted with PDX5950 and treated as described in Figure 3a. Group sizes (n) are indicated in the risk table; log-rank test results: ***P < 0.001; ns, not significant. **d** MRI-quantified tumor volumes at week 4 post-treatment. *P < 0.05. **e** Left: Representative IHC staining for cleaved caspase-3 in PDX5950 tumors. Right: Quantification of cleaved caspase-3-positive cells. Data are represented as mean ± SEM. *P < 0.05; **P < 0.01.

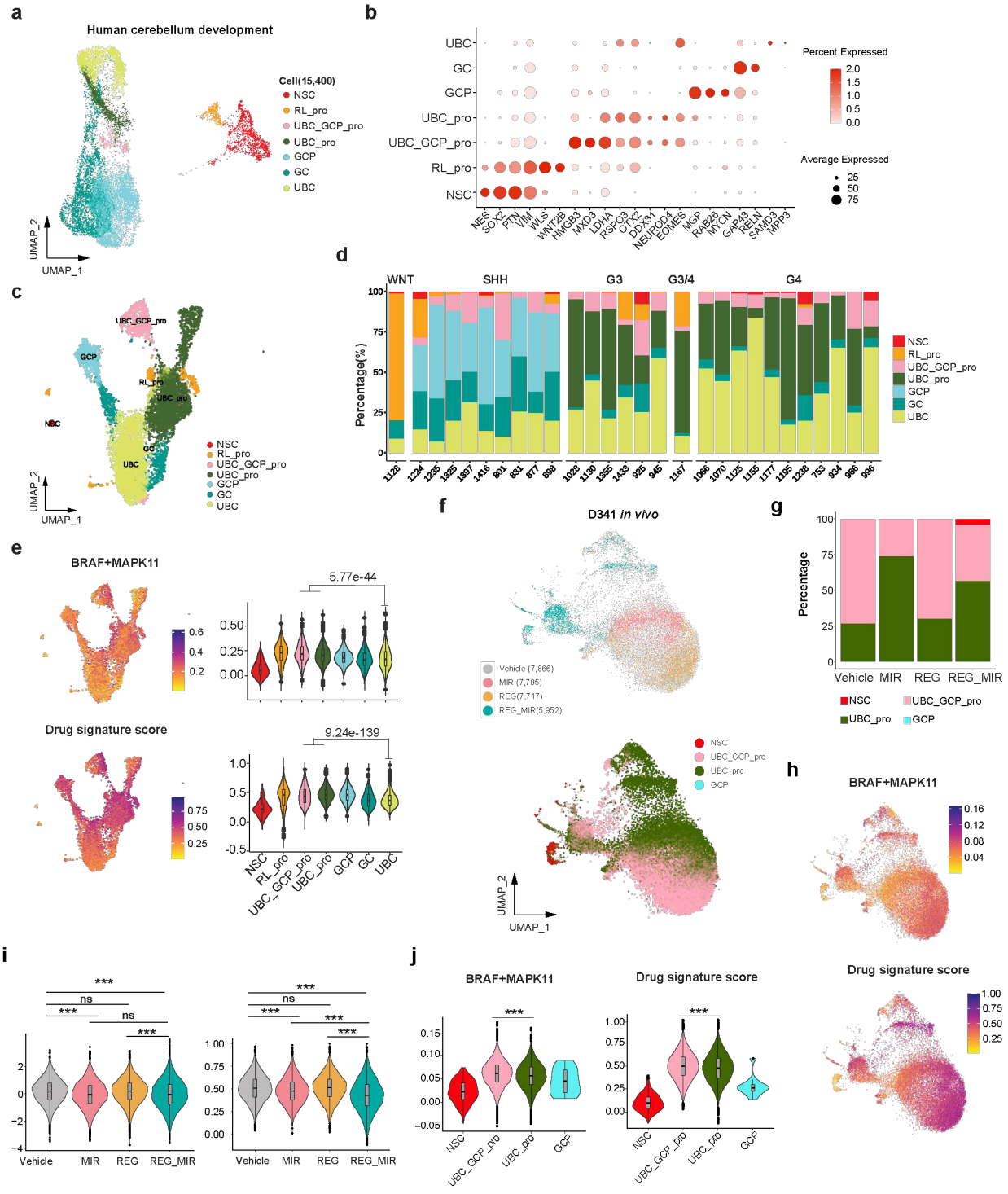
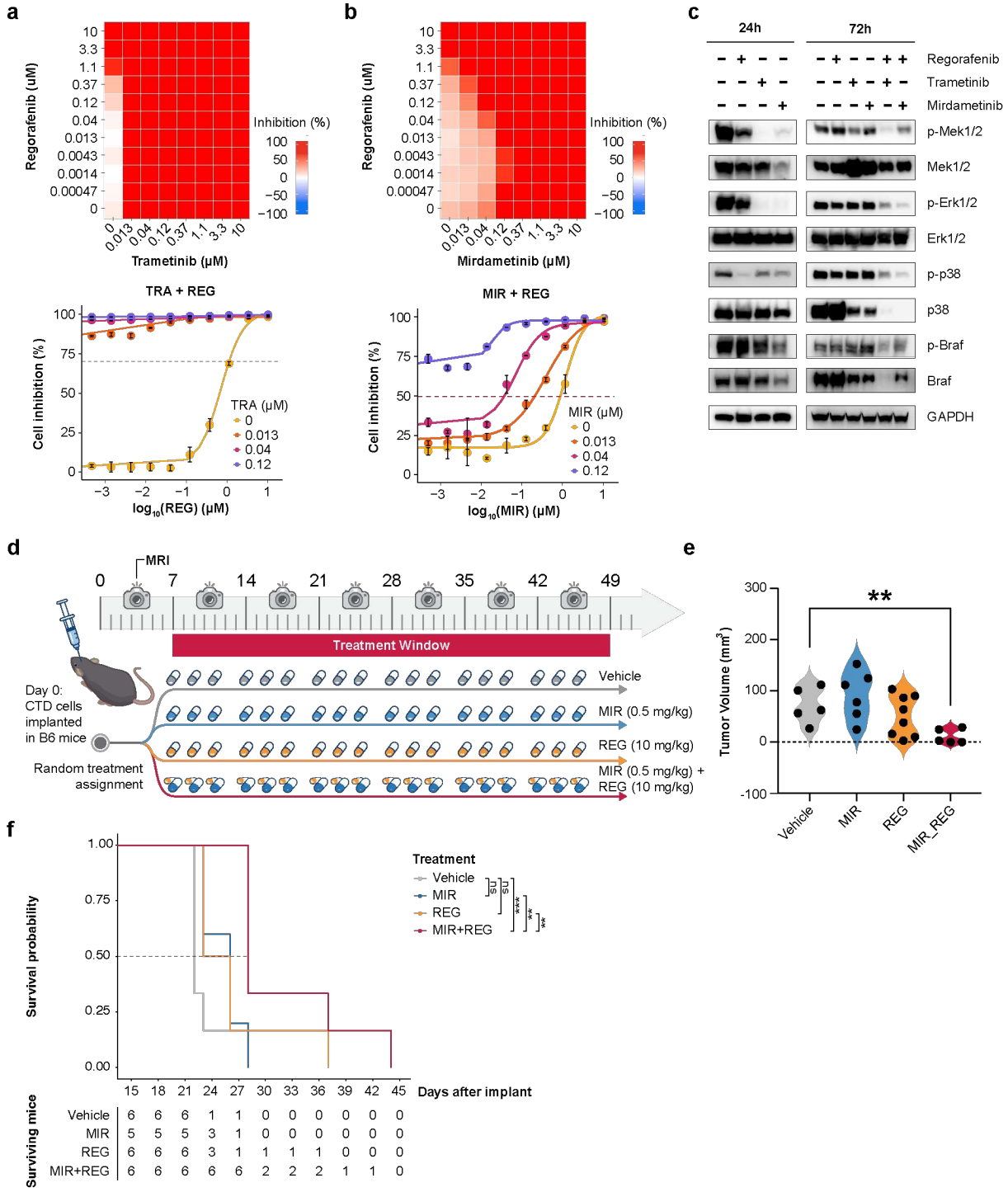


Figure 5. MEK inhibitor and regorafenib combination therapy targets on UBC_GCP common progenitor and UBC progenitor like tumor cells. a Re-annotation of the normal glutamatergic neuronal lineage, projected onto a UMAP embedding using scRNA-seq data from

Luo et al. **b** Expression patterns of key marker genes defining glutamatergic lineage cell states. **c** Cell state annotation of Medulloblastoma tumor cells (patient scRNA-seq data, GSE156053*;* *Riemondy et al*.) using the normal developmental reference from A. Visualization restricted to tumor cells. **d** Proportional distribution of tumor cell states across medulloblastoma patient subgroups. **e** Feature and violin plots showing driver combination activities and predicted drug sensitivity scores within tumor populations. **f** UMAP visualization of orthotopically implanted D341 tumor cells (in CD-1 mice) from treated mice, annotated with cell states using the normal developmental reference. **g** Proportional distribution of tumor cell states across treatment groups. **h-j** Single-cell feature plots (**h**) and violin plots (**i**, **j**) of driver activities and drug sensitivity scores across treatment arms (**i**) and predicted cell states (**j**).



1580

1581 **Figure 6. The combination of MEK inhibitor and regorafenib is effective in CTD, an**

1582 **immunocompetent syngenetic mouse model of G3 MB. a-b** Top: Heatmap of the CTD

1583 syngenetic mouse tumor cell viability treated with regorafenib and MEK inhibitor combinations.

Bottom: Dose-response curves of regorafenib with fixed concentrations of trametinib (left) or mirdametinib (right). **c** Western blot analysis of total and phosphorylated Mek, Erk, p38, and Braf in CTD cells following treatment at indicated time points. **d** Schematic of experimental design for drug administration and MRI imaging in C57BL/6J mice (created with BioRender.com). Seven days after intracranial implantation of CTD cells, mice were randomized into four treatment groups and treated three times per week for six weeks with vehicle (p.o.), mirdametinib (0.5 mg/kg p.o.), regorafenib (10 mg/kg p.o.), or the combination. **e** MRI-measured tumor volumes across treatment groups. Unpaired two-sided t tests were used; **P < 0.01. **f** Kaplan–Meier survival curves for mice treated as described in (D). Group sizes (n) are indicated in the risk table; log-rank test results: *P < 0.05, **P < 0.01, ***P < 0.001, ns, not significant.

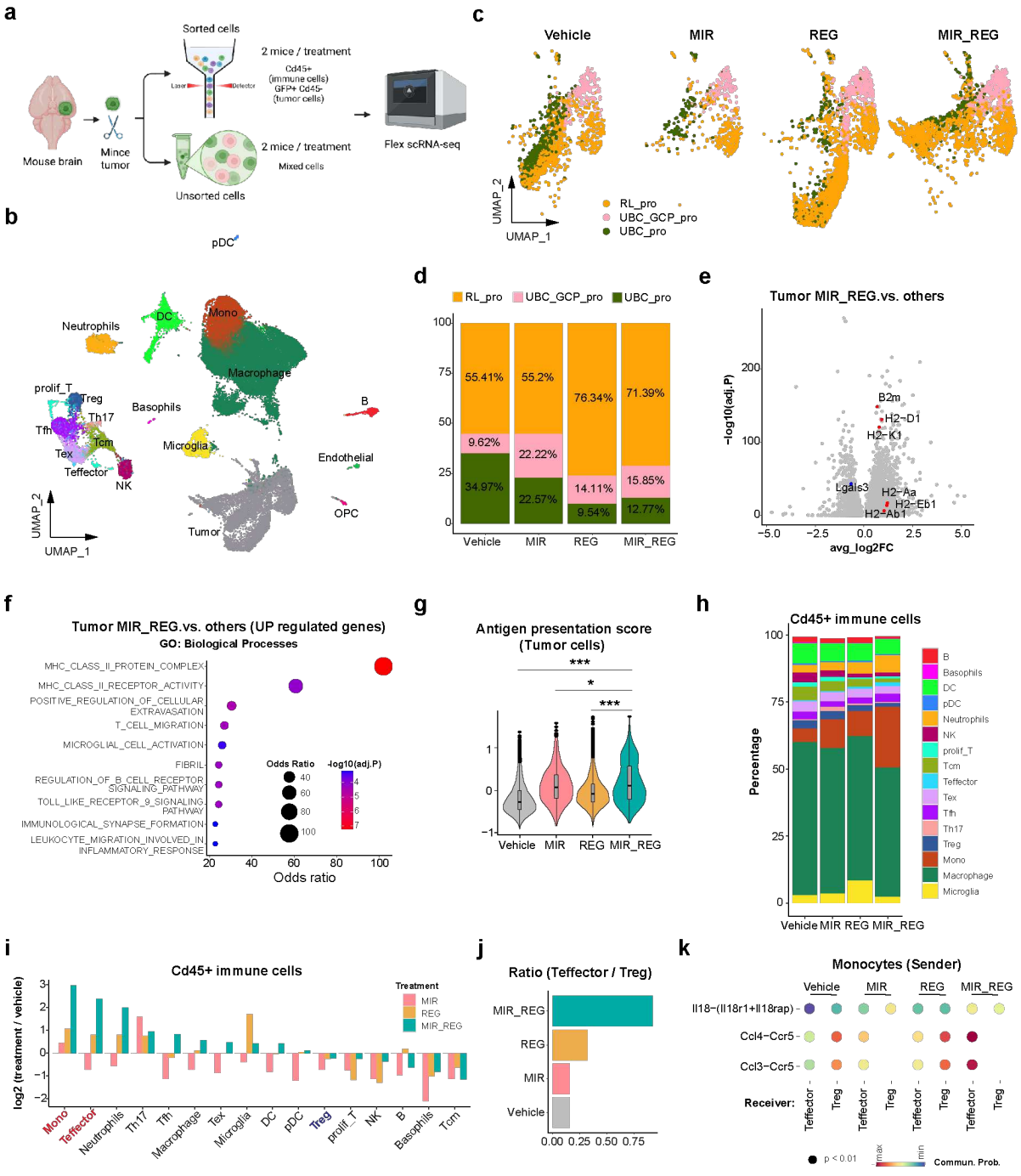


Figure 7. MEK inhibition combined with regorafenib remodels tumor cell states and the tumor microenvironment in the CTD syngenetic mouse model. **a** Schematic of experimental design for generating scRNA-seq data from the CTD syngeneic model preclinical study (created with BioRender.com). **b** UMAP visualization of the cells from the CTD model treated with monotherapy or combination therapy *in vivo*, with cells colored by their annotated cell types. **c**

UMAP plot of tumor cell states in the four treatment groups. **d** Proportional distribution of tumor cell states across treatment groups. **e** Volcano plot of differentially expressed genes in tumor cells from the MIR_REG combination group versus other treatments. **f** Functional enrichment of top upregulated genes (avg_log2FC > 1, adjusted p < 0.05) in tumor cells from the MIR_REG combination group. **g** Antigen presentation module scores in tumor cells across treatment groups; two-sided t tests were used to compare combination treatment with other groups. *P < 0.05, **P < 1.0e-10, ***P < 1.0e-20. **h** Proportional distribution of Cd45+ immune cells across treatment groups. **i** Log2 fold-change in abundance of immune cell populations for each treatment group relative to the vehicle control. **j** Ratio of T effector (Teffector) to T regulatory (Treg) cells across treatment groups. **k** CellChat-inferred ligand–receptor communication probabilities from monocytes to Teffector and Treg cells.

Supplementary Files

This is a list of supplementary files associated with this preprint. Click to download.

- SupplementaryTables.xlsx
- SupplementatyInformation.pdf